Phase Diagrams and Stability of Lead-Free Halide Double Perovskites $Cs_2BB'X_6$, B = Sb, Bi, B′ = Cu, Ag, Au and X = Cl, Br, I

Marina R. Filip,[†] Xinlei Liu,[†] Anna Miglio,[‡] Geoffroy Hautier,[‡] and Feliciano Giustino[*,†]

†*Department of Materials, University of Oxford, Parks Road OX1 3PH, Oxford, UK*

‡*Institute of Condensed Matter and Nanosciences, Chemin des Étoiles 8/L7.03.01 1348 Louvain-la-Neuve*

E-mail: feliciano.giustino@materials.ox.ac.uk

Abstract

Lead-free pnictogen/noble metal halide double perovskites $Cs_2BiAgCl_6$, $Cs_2BiAgBr_6$ and $Cs_2SbAgCl_6$ are some of the most promising environmentally friendly alternatives to lead-halide perovskites. However, due to their relatively large band gaps (1.9 to 2.2 eV), they are not yet competitive candidates for use in photovoltaic devices. In this work, we perform a systematic study of the thermodynamic stability of the entire family of $Cs_2BB'X_6$ compounds (B = Bi, Sb, B′ = Cu, Ag, Au and X = Cl, Br, I), and we explore the possibility of chemical mixing as a route to stabilize pnictogen/noble metal halide perovskites with low band gaps. Our calculations indicate that $Cs_2BiAg_{1-x}Cu_xCl_6$ mixes should be amenable to synthesis, and could reduce the band gap down to 1.6-1.9 eV.

Table of Contents Image

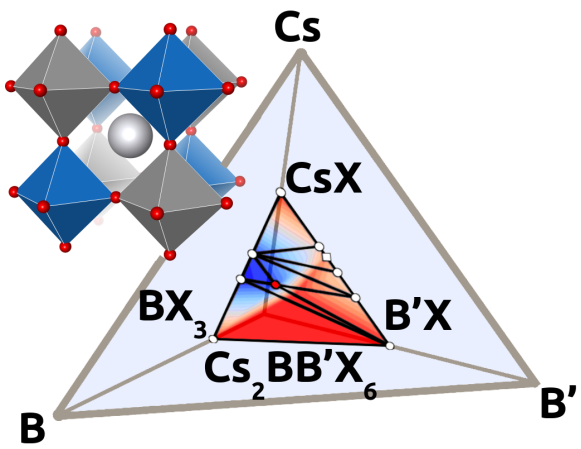

Keywords: Double halide perovskites, Lead-free perovskites, Phase Diagrams, Stability

Introduction

Lead-halide perovskites are emerging as one of the most promising classes of optoelectronic materials of the last decade. Solar cells based on organic-inorganic lead-iodide perovskites have experienced a rapid rise in power conversion efficiency since the first report in 2009 (3.9%),[1] up to a record efficiency of 22.1%.[2] The fast-paced progress of perovskite solar cells is linked to the remarkable optoelectronic properties of organic-inorganic lead-halide perovskites: optimum and tunable direct band gaps in the visible range,[3,4] low effective masses,[5] low exciton binding energies[6] and long carrier diffusion lengths and recombination lifetimes.[7]

Recently, much effort has been dedicated to designing and synthesizing new halide perovskites which are related to the prototypical $CH_3NH_3PbI_3$. This activity is motivated on the one hand by the need to improve the stability and the performance of perovskite solar cells,[3,8,9] and on the other hand by the toxicity concerns over the presence of Pb.[10] Starting from $CH_3NH_3PbI_3$, partial substitution of the $CH_3NH_3^+$ cation by $CH(NH_2)_2^+$,[11,12] Cs[3] and Rb[8] in conjunction with the partial substitution of I by Br,[3,8] leads to a change in the band gap by more than 1 eV, and to a significant improvement of the stability of the compounds. Furthermore, the substitution of Pb^{2+} by Sn^{2+} is an attractive option to redshift the band gap and to reduce toxicity.[13,14] However, the formation of pure Sn-based perovskites is problematic due to the oxidation of Sn^{2+} to Sn^{4+}.[13] This issue can be resolved either by partial substitution of Pb by Sn, which stabilizes the Sn-perovskites and gives access to a broad range of optical gaps,[9] or by exploring the Periodic Table for other suitable Pb replacements.

Both experimental and theoretical studies have investigated extensively the possibility to design lead-free halide perovskites by aliovalent, homovalent and heterovalent substitution.[15] The aliovalent replacement of Pb leads to significant structural changes and non-perovskite compounds. Thus, the incorporation of a +3 metal like Bi or Sb forms halides with the

structure of a perovskite-like chain of face-sharing octahedra (as in $Cs_3Bi_2I_9$[16] or $Cs_3Sb_2I_9$[17]), while a +4 metal leads to the formation of so-called 'vacancy ordered double perovskites' (as in Cs_2SnI_6[18,19] and Cs_2PdBr_6[20]). These compounds are highly stable and have optical bandgaps of 2-2.2 eV ($Cs_3Bi_2I_9$ and $Cs_3Sb_2I_9$) or ∼1.6 eV (Cs_2SnI_6 and Cs_2PdBr_6). However, their band edges exhibit flat profiles as a result of the lack of connectivity between the metal-halide octahedra, thus hindering the transport of photogenerated charge carriers. In principle, the perovskite structure can be retained by using homovalent Pb replacements. In practice, however, the substitution of Pb by other divalent metals in the Periodic Table leads either to unstable perovskites or to stable semiconductors with band baps larger than 2.7 eV,[21,22] such as halide perovskites based on the alkali earth metals Ca, Sr or Ba.[23–25]

The most successful strategy so far in the design of lead-free halide perovskites is the heterovalent substitution of lead.[26–38] In this approach, the Pb^{2+} cations are replaced by a +1 and a +3 metal, so as to maintain charge neutrality.[28,29] The structure thus formed is an ordered double perovskite (shown in Figure 1a), and has a general chemical formula of $A_2BB'X_6$, where A is a monovalent organic or inorganic cation, X is the halogen anion and B and B′ are +3 and +1 cations. High-throughput studies exploring the heterovalent substitution of Pb reveal a number of promising new semiconductor candidates for lead-free light absorbers.[39–41]

The halide double perovskite light absorbers proposed so far can be categorized in four separate groups of compounds, based on the combinations of B and B′ cations employed: pnictogen/alkali metals (B = Bi^{3+} and B′ = Na^+, K^+), pnictogen/post transition metals (B = Bi^{3+}, Sb^{3+}, and B′ = Tl^+, In^+), post transition/noble metals (B = In^{3+}, Ga^{3+}, and B′ = Cu^+, Ag^+) and pnictogen/noble metals (B = Bi^{3+}, Sb^{3+}, and B′ = Cu^+, Ag^+, Au^+). The pnictogen/alkali double perovskites (for example $(CH_3NH_3)_2BiKCl_6$[30,31] and $Cs_2BiNaCl_6$[28,39]) are large band gap semiconductors, and are not suitable visible light absorbers. On the other hand, post transition metals are more promising as +1 cations from an

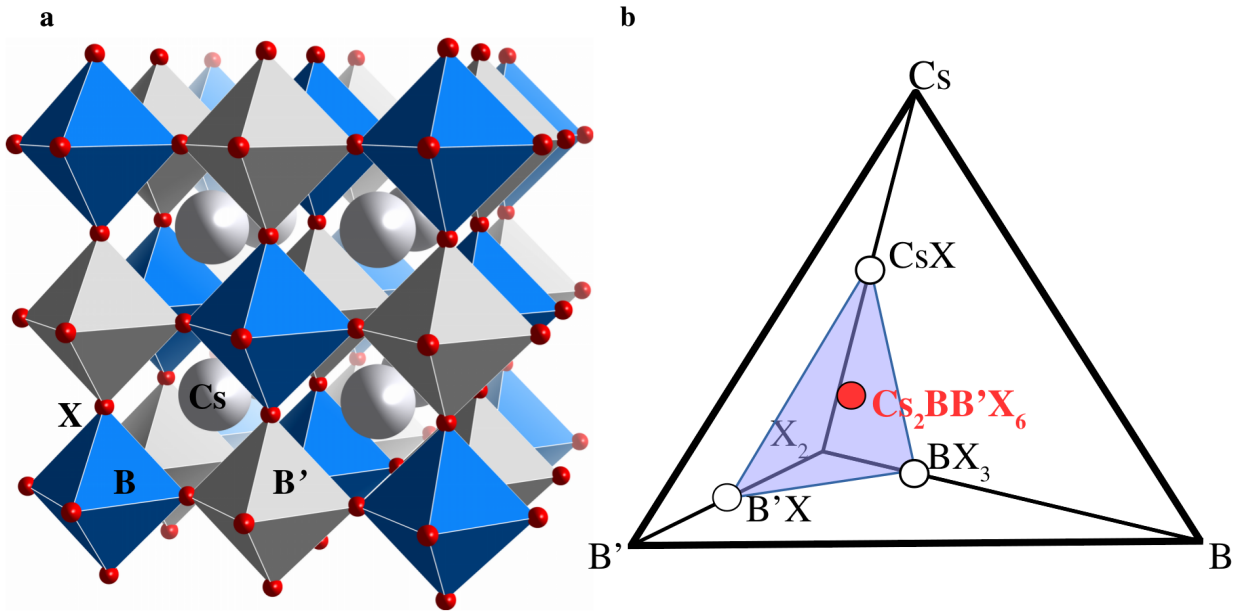

Figure 1: **Quaternary halide double perovskites**. **a**. Polyhedral model of the double perovskite structure. The grey spheres represent the Cs atoms, the blue octahedra are centered at the B-site, with B = Bi, Sb, the grey octahedra are centered at the B′-site, with B′ = Cu, Ag, Au, and the red spheres represent halogen anions X = Cl, Br, I. **b**. Schematic representation of the quaternary phase diagram. The corners of the diagram are labeled by the elemental compositions of the double perovskite. Each point of the tetrahedron represents a composition of Cs, B, B′ and X. The white disks mark the position of the precursors CsX, B′X and BX_3 on the quaternary phase diagram, and the red disk represents the quaternary double perovskite. The four compositions marked on the phase diagram are coplanar, as highlighted by the light blue triangle representing the ternary phase diagram of the solid state reaction.

electronic structure point of view. $(CH_3NH_3)_2BB'X_3$ (with B = Bi and Sb, B′ = Tl, In and X = Cl, Br, I) have remarkably similar band structures to the lead-halide perovskites.[31,38,42,43] For example, $(CH_3NH_3)_2BiTlBr_3$ has recently been synthesized,[31] however the toxicity of Tl rules out this compound as an environmentally-friendly alternative to lead-halide perovskites. $(CH_3NH_3)_2BiInBr_6$, while non-toxic, has not yet been synthesized due to the oxidation of In^+ into In^{3+}.[38,43] In fact, In^{3+} can be successfully incorporated into a halide double perovskite, as demonstrated by the synthesis of $Cs_2InAgCl_6$.[32] Several double perovskites based on post transition metals In and Ga and noble metals Ag and Cu have been recently proposed,[37,39] however due to the presence of transition-metal *d*-states, the valence band top in this family of compounds exhibits a flat profile, and the compounds are prone to problematic mid-gap

defects.[32] On the other hand, the replacement of In^{3+} by pnictogens Bi and Sb restores the dispersive valence band top.[28,29]

The hypothetical pnictogen-noble metal halide double perovskites based on Bi, Sb and Cu, Ag, Au proposed in Ref. 28 have indirect band gaps which span the entire visible spectrum, and exhibit low effective masses.[28] Of the 18 double perovskites proposed,[28] three pure compounds ($Cs_2BiAgCl_6$,[27–29] $Cs_2BiAgBr_6$[26,27,29] and $Cs_2SbAgCl_6$[33]) and one mixed compound ($Cs_2Bi_{1-x}Sb_xAgBr_6$, x$\leq$0.375) have been synthesized[36] so far. They are highly stable crystals under environmental conditions, and exhibit indirect band gaps between 1.9 and 2.3 eV.[26,28,29,33,36] In particular, $Cs_2BiAgBr_6$ does not appear to be prone to problematic defects, according to *ab initio* calculations, and should be a naturally good p-type conductor due to its tendency to accept Ag vacancies as shallow defects.[44] In addition, the possibility of incorporating organic cations into the pnictogen-noble metal double perovskite proposed in Ref. 28 was recently demonstrated by the synthesis of $(CH_3NH_3)_2BiAgBr_6$.[34]

The indirect character of the band gap of pnictogen-noble metal halide double perovskites may suggest that these materials are not suitable for thin film solar cells. Nonetheless, given that silicon is the prototypical indirect gap semiconductor, and currently the most dominant photovoltaic material, it is possible that this family of double perovskites will find application in conventional crystalline solar cells, tandem devices,[26] or photodetectors.[45] Of the compounds synthesized thus far, $Cs_2BiAgBr_6$ is the first to be incorporated as a light absorber in a lead-free inorganic halide perovskite solar cell with a power conversion efficiency of 2.5%.[46] While $Cs_2BiAgCl_6$, $Cs_2SbAgCl_6$ and $Cs_2BiAgBr_6$ absorb light from the yellow and red regions of the visible spectrum, theoretical predictions[28] suggest that within this family of double perovskites there is potential to design a light absorber with a band gap close to the Shockley-Queisser limit of 1.4 eV.[47] In particular, the synthesis of the mixed $Cs_2Bi_{1-x}Sb_xAgBr_6$[36] demonstrates that $Cs_2BiAgBr_6$ can be used as template for synthesizing mixed pnictogen double perovskites with reduced band gaps. Therefore, in this work we aim

to explore this idea for the entire family of pnictogen/noble metal double perovskites, and we investigate the possibility of tuning the band gap by chemical mixing.

We address this question from a theoretical viewpoint by using density functional theory (DFT).[48] Recent work by Ong et al.[49,50] demonstrated that it is possible to assess the thermodynamic stability of a compound using DFT by constructing its compositional phase diagram. In this approach, the stability of a compound is studied not only against the decomposition into its constituent elements, but also against all possible decomposition reactions. This approach has become popular in the context of large scale high-throughput computational design, where it is used as an essential screening step.[22,51,52] In this work, we perform a systematic theoretical investigation of the stability of double perovskite compounds proposed in Ref. 28 using the method of Ong et al.[49,50] From our analysis we find that $Cs_2BiAgCl_6$, $Cs_2BiAgBr_6$, and $Cs_2SbAgCl_6$ are stable against decomposition, in excellent agreement with experimental observations. In addition, we investigate how $Cs_2BiAgCl_6$, $Cs_2BiAgBr_6$ and $Cs_2SbAgCl_6$ can be used to stabilize mixed double perovskites such as $Cs_2BiAg_{1-x}Cu_xCl_6$, $Cs_2SbAg_{1-x}Cu_xCl_6$, $Cs_2BiAg(Br_{1-x}I_x)_6$ and $Cs_2SbAg(Cl_{1-x}Br_x)_6$.

Methodology

One of the methods of synthesis for $Cs_2BiAgCl_6$, $Cs_2BiAgBr_6$ and $Cs_2SbAgCl_6$ is through solid state reaction.[28,29,33] In this approach, precursor salts of CsX, BX_3 and AgX (B = Bi, Sb and X = Cl, Br) are ground together and heated to high temperature in a vacuum sealed ampoule, so as to facilitate the following reaction:

$$2\ \mathrm{CsX} + \mathrm{BX_3} + \mathrm{AgX} \rightarrow \mathrm{Cs_2BAgX_6}, \tag{1}$$

This is an isobaric, isothermal and closed process, and is best described thermodynamically by the Gibbs free energy,[49] $G(T, P, \{N_i, i = \overline{1, M}\}) = U(T, P, \{N_i, i = \overline{1, M}\}) -$

$TS(T, P, \{N_i, i = \overline{1, M}\}) + PV(T, P, \{N_i, i = \overline{1, M}\})$, where $U(T, P, \{N_i, i = \overline{1, M}\})$ is the total energy of the system, $V(T, P, \{N_i, i = \overline{1, M}\})$ is the volume, $S(T, P, \{N_i, i = \overline{1, M}\})$ is the entropy, T is the temperature, P is the pressure and N_i is the number of atoms of each of the M species in the system.

The formation of a multinary compound from its M constituent elements is probed by calculating the change in the Gibbs potential:[49]

$$\Delta G = \Delta U + P\Delta V - T\Delta S, \tag{2}$$

where the change in the Gibbs potential is defined as $\Delta G = G(\text{compound}) - G(\text{elements})$. At a given temperature or pressure, $\Delta G_{T,P}(\{N_i, i = \overline{1, M}\})$ defines the compositional phase diagram. ΔG outlines a convex shape for all compositions corresponding to stable compounds in the phase diagram. In practice the compositional phase digram is constructed using the convex hull method.[49]

In this study we are interested in obtaining the compositional phase diagrams of quaternary systems of the type Cs - B - B′ - X (with B = Sb, Bi, B' = Cu, Ag, Au and X = Cl, Br, I) from density functional theory (DFT). Therefore, in our calculations we will use the approximate approach proposed by Ong et al, whereby the compositional phase diagrams are constructed at $T = 0$ K and $P = 0$ atm. In these conditions, the change in the Gibbs free energy from Eq. 2 becomes equivalent to $\Delta G = \Delta U$,[49] thereby not including the effects of entropy and pressure into our analysis.

Computational Setup

First principles calculations. All the results presented in this manuscript were obtained from density functional theory (DFT) calculations,[48] as implemented in the Quantum Espresso package.[53] In our study we use both the local density approximation (LDA)[54]

and the generalized gradient approximation in the Perdew-Burke-Erzenhof parametrization (PBE)[55] for the exchange-correlation functional. For Bi, Sb, Cu, Ag, Au, Cl, Br and I we use scalar-relativistic ultrasoft pseudopotentials, while for Cs we use norm-conserving non-relativistic pseudopotentials. For both LDA and PBE calculations we consider the following valence electronic configurations: $5s^2 5p^6 6s^1$ for Cs, $nd^{10}(n+1)s^2(n+1)p^3$ (with $n = 5$ for Bi and $n = 4$ for Sb), $nd^{10}(n+1)s^1$ (with $n = 3$ for Cu, $n = 4$ for Ag, and $n = 5$ for Au), and ns^2np^5 (with $n = 3$ for Cl, $n = 4$ for Br, and $n = 5$ for I). All pseudopotentials can be found in the Quantum Espresso and Theos libraries.[56]

The total energy is converged separately for each of the constituting elements with respect to the plane wave cutoffs. In addition, we converge the total energy with respect to the density of the **k**-point mesh separately for each compound represented in the phase diagram. A calculation is considered converged when total energy is accurate within 5 meV/atom. For all final calculations we use a kinetic cutoff of 80 Ry for the wave functions and 400 Ry for the charge density.

Structural data provenance. To construct the phase diagrams we obtain the structural information for all the components of the phase diagram from the Materials Project database. For a particular set of elements, we select all compounds given by the Phase Diagram App in the Materials Project.[57] If a compound is reported with multiple structures we select the structure which is most stable. In addition, we complete the phase diagrams for each of the possible quaternary systems, by chemical substitution. For example, if $CsCu_2Cl_3$ is a stable compound in the phase diagram of the Cs - Bi - Cu - Cl, we make sure that a corresponding CsB'_2X_3-type compound is included in all the phase diagrams of all other quaternary systems, even if it is not reported in the Materials Project. Using this approach we construct each of the phase diagrams using 35 compounds, including the quaternary double perovskite and the elemental compounds (compiling a total of 220 distinct compounds). We emphasize that for all compounds included in the phase diagrams we did not use the total energies

stored in the Materials Project database, but instead all the total energies were recalculated within LDA and PBE using the Quantum Espresso package. The complete list of all the compounds included in our phase diagrams are given in Tables1 and 2, along with their calculated formation energies. All phase diagrams and formation energies were calculated using the Pymatgen package.[58] For all halide double perovskites the crystal structures were optimized using both LDA and PBE starting from both the face-centered cubic structure reported in Ref. 28, and from the orthorhombic *Pnma* structure, and the lowest total energy structure was chosen for the calculation of phase diagrams. In addition, for all gaseous elements of the quaternary phase diagrams (such as Cl_2, Br_2 and I_2), the total energies were calculated for the structures provided in the Materials Project database. While in Materials Project total energies calculated for O_2, F_2, Cl_2 and N_2 are typically corrected so that they match experimental formation energies, as described in Ref. 59, we chose not to include this correction for the sake of consistency. Given that the highest decomposition energies in our phase diagrams correspond to reactions that do not include gaseous compounds, this choice does not affect our final results.

Decomposition energies. To calculate the lowest decomposition energies for the stable compounds (shown in Figure 2 and Table 3) we consider that the double perovskite $Cs_2BB'X_6$, can decompose into at most four of the products found in the phase diagram of each quaternary system. There are 5047 possible decomposition reactions from the quaternary phase diagram. For the stable double perovskites, the results shown in Figure 2 and Table 3 represent the lowest decomposition energies calculated. For the analysis of the pseudo-ternary phase diagrams we follow a similar approach. In this case, there are only 17 possible decomposition reactions, and all the decomposition energies and reactions are listed in Tables 4 and 5.

Total energy of the mixed double perovskites $Cs_2BiAg_{0.875}Cu_{0.125}Cl_6$ and $Cs_2BiAg_{0.75}Cu_{0.25}Cl_6$. We construct the ordered structure of the mixed double perovskites

by substituting one of the Ag cations in supercells of 8 and 16 octahedra, respectively. The 8 octahedra unit cell is constructed starting from the experimental $Fm\bar{3}m$ space group, atomic positions and lattice parameters given in Ref. 28. The 16 octahedra unit cell is obtained by doubling the 8 octahedra cell along the c axis. Within this framework there is only one structural configuration possible, by symmetry. We obtain the final structure by structural optimization of the atomic positions and lattice parameters. For the structural optimization we use a Γ-centered **k**-point grid of $4 \times 4 \times 2$ and $4 \times 4 \times 4$ for $Cs_2BiAg_{0.875}Cu_{0.125}Cl_6$ and $Cs_2BiAg_{0.75}Cu_{0.25}Cl_6$, respectively and the plane wave cutoffs of 80 Ry and 400 Ry, as described above.

Band gap of mixed double perovskites. We evaluate whether the mixed noble metal compounds are likely to improve the efficiency of lead-free halide double perovskite solar cells by calculating their band gaps. In general, the band gap is only an approximate descriptor for the light absorbing properties of a semiconductor. A more accurate evaluation of the potential of a new compound as a light absorber is the calculation of the optical absorption spectrum and the spectroscopic limited maximum efficiency (SLME)[60] metric. However, given that these compounds all exhibit an indirect band gap, the *ab initio* calculation of the optical absorption spectrum must include phonon-assisted optical transitions,[61,62] and goes beyond the scope of the present work. Here we are interested in identifying routes to reduce the band gap of three already synthesized semiconductors, and therefore we focus on calculating the dependence of the band gap on the mixing concentration.

We calculate the change in band gap with the concentration of Cu for the mixed noble-metal double perovskite $Cs_2BiAg_{1-x}Cu_xCl_6$ using the virtual crystal approximation, as described in Ref. 63. This approach assumes that the noble-metal sites are occupied by 'virtual' atoms with mixed Ag and Cu character. For these calculations we used norm-conserving pseudopotentials without non-linear core-corrections, and a cutoff of 100 Ry. In order to take into account the large spin-orbit coupling effect in Bi-based double perovskites we use

fully-relativistic pseudopotentials for Bi and Ag. The pseudopotentials for Cs, Cu and Cl were taken from the Quantum Espresso library, while the Bi and Ag pseudopotentials were constructed as described in Ref. 29.

For each concentration of Cu we relaxed the structures while keeping the lattice parameters fixed. The lattice parameters of the mixed double perovskites at each concentration were obtained by linear interpolation between the calculated lattice parameters of $Cs_2BiAgCl_6$ and $Cs_2BiCuCl_6$. For all virtual crystal calculations we consider only the cubic phase of the double perovskites. For completeness, in Figure 5g we show both the band gaps calculated from the virtual crystal approximation and the band gaps calculated for the ordered structures. We find that for a concentration of Cu of 25%, the band gap of the ordered structure is larger than the band gap of the disordered mixed compound by 0.3 eV. This difference is similar to that obtained for the case of Pb-Sn mixes in Ref. 9

Table 1: Calculated formation energies for all compounds included in the convex hull of the Bi-based double perovskites. Formation energies are calculated with respect to the elemental compounds Cs, Bi, B′ = Cu, Ag, Au and X_2 (X = Cl, Br, I). All energies are expressed in eV/atom.

General	Cs-Bi-Cu-Cl		Cs-Bi-Cu-Br		Cs-Bi-Cu-I		Cs-Bi-Ag-Cl		Cs-Bi-Ag-Br		Cs-Bi-Ag-I		Cs-Bi-Au-Cl		Cs-Bi-Au-Br		Cs-Bi-Au-I	
formula	LDA	PBE	LDA	PBE	LDA	PBE	LDA	PBE	LDA	PBE	LDA	PBE	LDA	PBE	LDA	PBE	LDA	PBE
Cs	0.000	0.000	0.000	0.000	0.000	0.000	0.000	0.000	0.000	0.000	0.000	0.000	0.000	0.000	0.000	0.000	0.000	0.000
B	0.000	0.000	0.000	0.000	0.000	0.000	0.000	0.000	0.000	0.000	0.000	0.000	0.000	0.000	0.000	0.000	0.000	0.000
B′	0.000	0.000	0.000	0.000	0.000	0.000	0.000	0.000	0.000	0.000	0.000	0.000	0.000	0.000	0.000	0.000	0.000	0.000
X_2	0.000	0.000	0.000	0.000	0.000	0.000	0.000	0.000	0.000	0.000	0.000	0.000	0.000	0.000	0.000	0.000	0.000	0.000
B_2B'	0.050	0.052	0.050	0.052	0.050	0.052	0.043	0.051	0.043	0.051	0.043	0.051	-0.120	-0.118	-0.120	-0.118	-0.120	-0.118
B_6X_7	-0.789	-0.744	-0.531	-0.559	-0.301	-0.350	-0.789	-0.744	-0.531	-0.559	-0.301	-0.350	-0.789	-0.744	-0.531	-0.559	-0.301	-0.350
BB'_2	0.159	0.120	0.159	0.120	0.159	0.120	0.008	-0.003	0.008	-0.003	0.008	-0.003	-0.091	-0.097	-0.091	-0.097	-0.091	-0.097
$BB'X_6$	-0.770	-0.709	-0.440	-0.485	-0.191	-0.229	-0.703	-0.638	-0.401	-0.444	-0.184	-0.239	-0.735	-0.679	-0.423	-0.476	-0.202	-0.250
BX_3	-1.062	-0.976	-0.714	-0.802	-0.448	-0.515	-1.062	-0.976	-0.714	-0.802	-0.448	-0.515	-1.062	-0.976	-0.714	-0.802	-0.448	-0.515
BX_5	-0.488	-0.469	-0.195	-0.273	0.007	-0.069	-0.488	-0.469	-0.195	-0.273	0.007	-0.069	-0.488	-0.469	-0.195	-0.273	0.007	-0.069
B'_2X_3	-0.572	-0.471	-0.264	-0.266	-0.046	-0.050	-0.462	-0.417	-0.242	-0.290	-0.104	-0.146	-0.086	-0.028	0.064	0.028	0.104	0.078
B′X	-0.474	-0.402	-0.223	-0.257	-0.130	-0.169	-0.426	-0.430	-0.203	-0.356	-0.139	-0.269	-0.173	-0.221	-0.008	-0.127	0.058	-0.055
$B'X_2$	-0.592	-0.528	-0.294	-0.332	-0.101	-0.137	-0.410	-0.364	-0.206	-0.259	-0.024	-0.078	-0.299	-0.267	-0.053	-0.132	0.008	-0.059
$B'X_3$	-0.430	-0.372	-0.281	-0.203	-0.176	-0.148	-0.277	-0.209	-0.213	-0.108	-0.153	-0.194	-0.313	-0.273	-0.093	-0.150	0.012	-0.073
Cs_2BX_6	-1.474	-1.386	-1.164	-1.168	-0.875	-0.884	-1.474	-1.386	-1.164	-1.168	-0.875	-0.884	-1.474	-1.386	-1.164	-1.168	-0.875	-0.884
$Cs_2B'X_3$	-1.574	-1.476	-1.309	-1.301	-1.077	-1.083	-1.562	-1.503	-1.324	-1.347	-1.114	-1.143	-1.397	-1.400	-1.182	-1.237	-1.015	-1.036
$Cs_2B'X_4$	-1.466	-1.395	-1.171	-1.190	-0.949	-0.943	-1.360	-1.315	-1.106	-1.146	-0.888	-0.931	-1.306	-1.260	-1.057	-1.098	-0.862	-0.901
Cs_3B	-0.476	-0.347	-0.476	-0.347	-0.476	-0.347	-0.476	-0.347	-0.476	-0.347	-0.476	-0.347	-0.476	-0.347	-0.476	-0.347	-0.476	-0.347
Cs_3B_2	-0.493	-0.428	-0.493	-0.428	-0.493	-0.428	-0.493	-0.428	-0.493	-0.428	-0.493	-0.428	-0.493	-0.428	-0.493	-0.428	-0.493	-0.428
$Cs_3B_2X_9$	-1.573	-1.520	-1.252	-1.286	-0.964	-0.996	-1.573	-1.520	-1.252	-1.286	-0.964	-0.996	-1.573	-1.520	-1.252	-1.286	-0.964	-0.996
Cs_3BX_6	-1.755	-1.686	-1.444	-1.462	-1.149	-1.170	-1.755	-1.686	-1.444	-1.462	-1.149	-1.170	-1.755	-1.686	-1.444	-1.462	-1.149	-1.170
$Cs_3B'_2X_{11}$	-1.105	-1.018	-0.827	-0.843	-0.617	-0.631	-1.040	-0.951	-0.796	-0.809	-0.619	-0.631	-1.075	-0.994	-0.820	-0.840	-0.642	-0.659
$Cs_3B'_2X_5$	-1.480	-1.408	-1.223	-1.230	-1.006	-1.023	-1.429	-1.380	-1.205	-1.233	-1.016	-1.045	-1.324	-1.306	-1.095	-1.149	-0.924	-0.968
Cs_5B_8	-0.394	-0.380	-0.394	-0.380	-0.394	-0.380	-0.394	-0.380	-0.394	-0.380	-0.394	-0.380	-0.394	-0.380	-0.394	-0.380	-0.394	-0.380
CsB	-0.501	-0.462	-0.501	-0.462	-0.501	-0.462	-0.501	-0.462	-0.501	-0.462	-0.501	-0.462	-0.501	-0.462	-0.501	-0.462	-0.501	-0.462
CsB_2	-0.476	-0.400	-0.476	-0.400	-0.476	-0.400	-0.476	-0.400	-0.476	-0.400	-0.476	-0.400	-0.476	-0.400	-0.476	-0.400	-0.476	-0.400
$CsBX_6$	-1.028	-0.954	-0.714	-0.727	-0.535	-0.552	-1.028	-0.954	-0.714	-0.727	-0.535	-0.552	-1.028	-0.954	-0.714	-0.727	-0.535	-0.552
CsB′	0.549	0.422	0.549	0.422	0.549	0.422	0.202	0.069	0.202	0.069	0.202	0.069	-0.208	-0.336	-0.208	-0.336	-0.208	-0.336
CsB'_2X_3	-1.054	-0.983	-0.805	-0.817	-0.617	-0.639	-0.982	-0.980	-0.785	-0.858	-0.642	-0.708	-0.704	-0.693	-0.538	-0.595	-0.458	-0.507
$CsB'X_2$	-1.283	-1.178	-1.022	-1.008	-0.794	-0.796	-1.291	-1.241	-1.060	-1.094	-0.859	-0.901	-1.035	-0.969	-0.844	-0.864	-0.706	-0.731
$CsB'X_3$	-1.234	-1.137	-0.961	-0.955	-0.707	-0.709	-1.225	-1.108	-0.950	-0.926	-0.720	-0.722	-1.146	-1.066	-0.893	-0.904	-0.708	-0.721
CsX	-2.059	-1.983	-1.800	-1.805	-1.541	-1.561	-2.059	-1.983	-1.800	-1.805	-1.541	-1.561	-2.059	-1.983	-1.800	-1.805	-1.541	-1.561
CsX_3	-1.195	-1.081	-1.020	-0.991	-0.835	-0.841	-1.195	-1.081	-1.020	-0.991	-0.835	-0.841	-1.195	-1.081	-1.020	-0.991	-0.835	-0.841
CsX_4	-0.994	-0.874	-0.805	-0.807	-0.677	-0.683	-0.994	-0.874	-0.805	-0.807	-0.677	-0.683	-0.994	-0.874	-0.805	-0.807	-0.677	-0.683
$Cs_2BB'X_6$	-1.437	-1.335	-1.118	-1.115	-0.828	-0.845	-1.432	-1.370	-1.130	-1.156	-0.862	-0.885	-1.317	-1.248	-1.036	-1.072	-0.798	-0.828

Table 2: Calculated formation energies for all compounds included in the convex hull of the Sb-based double perovskites. Formation energies are calculated with respect to the elemental compounds Cs, Sb, B′ = Cu, Ag, Au and X_2 (X = Cl, Br, I). All energies are expressed in eV/atom.

General	Cs-Sb-Cu-Cl		Cs-Sb-Cu-Br		Cs-Sb-Cu-I		Cs-Sb-Ag-Cl		Cs-Sb-Ag-Br		Cs-Sb-Ag-I		Cs-Sb-Au-Cl		Cs-Sb-Au-Br		Cs-Sb-Au-I	
formula	LDA	PBE	LDA	PBE	LDA	PBE	LDA	PBE	LDA	PBE	LDA	PBE	LDA	PBE	LDA	PBE	LDA	PBE
Cs	0.000	0.000	0.000	0.000	0.000	0.000	0.000	0.000	0.000	0.000	0.000	0.000	0.000	0.000	0.000	0.000	0.000	0.000
B	0.000	0.000	0.000	0.000	0.000	0.000	0.000	0.000	0.000	0.000	0.000	0.000	0.000	0.000	0.000	0.000	0.000	0.000
B′	0.000	0.000	0.000	0.000	0.000	0.000	0.000	0.000	0.000	0.000	0.000	0.000	0.000	0.000	0.000	0.000	0.000	0.000
X_2	0.000	0.000	0.000	0.000	0.000	0.000	0.000	0.000	0.000	0.000	0.000	0.000	0.000	0.000	0.000	0.000	0.000	0.000
B_2B'	0.036	0.060	0.036	0.060	0.036	0.060	0.088	0.119	0.088	0.119	0.088	0.119	-0.107	-0.078	-0.107	-0.078	-0.107	-0.078
B_6X_7	-0.598	-0.549	-0.343	-0.363	-0.136	-0.174	-0.598	-0.549	-0.343	-0.363	-0.136	-0.174	-0.598	-0.549	-0.343	-0.363	-0.136	-0.174
BB'_2	0.008	0.015	0.008	0.015	0.008	0.015	0.132	0.128	0.132	0.128	0.132	0.128	0.066	0.064	0.066	0.064	0.066	0.064
$BB'X_6$	-0.686	-0.618	-0.356	-0.401	-0.120	-0.162	-0.617	-0.546	-0.316	-0.354	-0.107	-0.167	-0.650	-0.586	-0.338	-0.387	-0.126	-0.172
BX_3	-0.928	-0.882	-0.549	-0.617	-0.318	-0.363	-0.928	-0.882	-0.549	-0.617	-0.318	-0.363	-0.928	-0.882	-0.549	-0.617	-0.318	-0.363
BX_5	-0.665	-0.651	-0.266	-0.362	0.011	-0.049	-0.665	-0.651	-0.266	-0.362	0.011	-0.049	-0.665	-0.651	-0.266	-0.362	0.011	-0.049
B'_2X_3	-0.572	-0.471	-0.264	-0.266	-0.046	-0.050	-0.462	-0.417	-0.242	-0.290	-0.104	-0.146	-0.086	-0.028	0.064	0.028	0.104	0.078
B′X	-0.474	-0.402	-0.223	-0.257	-0.130	-0.169	-0.426	-0.430	-0.203	-0.356	-0.139	-0.269	-0.173	-0.221	-0.008	-0.127	0.058	-0.055
$B'X_2$	-0.592	-0.528	-0.294	-0.332	-0.101	-0.137	-0.410	-0.364	-0.206	-0.259	-0.024	-0.078	-0.299	-0.267	-0.053	-0.132	0.008	-0.059
$B'X_3$	-0.430	-0.372	-0.281	-0.203	-0.176	-0.148	-0.277	-0.209	-0.213	-0.108	-0.153	-0.194	-0.313	-0.273	-0.093	-0.150	0.012	-0.073
Cs_2BX_6	-1.497	-1.396	-1.168	-1.160	-0.864	-0.859	-1.497	-1.396	-1.168	-1.160	-0.864	-0.859	-1.497	-1.396	-1.168	-1.160	-0.864	-0.859
$Cs_2B'X_3$	-1.574	-1.476	-1.309	-1.301	-1.077	-1.083	-1.562	-1.503	-1.324	-1.347	-1.114	-1.143	-1.397	-1.400	-1.182	-1.237	-1.015	-1.036
$Cs_2B'X_4$	-1.466	-1.395	-1.171	-1.190	-0.949	-0.943	-1.360	-1.315	-1.106	-1.146	-0.888	-0.931	-1.306	-1.260	-1.057	-1.098	-0.862	-0.901
Cs_3B	-0.462	-0.330	-0.462	-0.330	-0.462	-0.330	-0.462	-0.330	-0.462	-0.330	-0.462	-0.330	-0.462	-0.330	-0.462	-0.330	-0.462	-0.330
Cs_3B_2	-0.493	-0.429	-0.493	-0.429	-0.493	-0.429	-0.493	-0.429	-0.493	-0.429	-0.493	-0.429	-0.493	-0.429	-0.493	-0.429	-0.493	-0.429
$Cs_3B_2X_9$	-1.516	-1.446	-1.192	-1.210	-0.898	-0.916	-1.516	-1.446	-1.192	-1.210	-0.898	-0.916	-1.516	-1.446	-1.192	-1.210	-0.898	-0.916
Cs_3BX_6	-1.696	-1.616	-1.386	-1.393	-1.094	-1.105	-1.696	-1.616	-1.386	-1.393	-1.094	-1.105	-1.696	-1.616	-1.386	-1.393	-1.094	-1.105
$Cs_3B'_2X_{11}$	-1.105	-1.018	-0.827	-0.843	-0.617	-0.631	-1.040	-0.951	-0.796	-0.809	-0.619	-0.631	-1.075	-0.994	-0.820	-0.840	-0.642	-0.659
$Cs_3B'_2X_5$	-1.480	-1.408	-1.223	-1.230	-1.006	-1.023	-1.429	-1.380	-1.205	-1.233	-1.016	-1.045	-1.324	-1.306	-1.095	-1.149	-0.924	-0.968
Cs_5B_8	-0.381	-0.372	-0.381	-0.372	-0.381	-0.372	-0.381	-0.372	-0.381	-0.372	-0.381	-0.372	-0.381	-0.372	-0.381	-0.372	-0.381	-0.372
CsB	-0.501	-0.462	-0.501	-0.462	-0.501	-0.462	-0.501	-0.462	-0.501	-0.462	-0.501	-0.462	-0.501	-0.462	-0.501	-0.462	-0.501	-0.462
CsB_2	-0.341	-0.250	-0.341	-0.250	-0.341	-0.250	-0.341	-0.250	-0.341	-0.250	-0.341	-0.250	-0.341	-0.250	-0.341	-0.250	-0.341	-0.250
$CsBX_6$	-1.172	-1.091	-0.785	-0.800	-0.485	-0.500	-1.172	-1.091	-0.785	-0.800	-0.485	-0.500	-1.172	-1.091	-0.785	-0.800	-0.485	-0.500
CsB′	0.549	0.422	0.549	0.422	0.549	0.422	0.202	0.069	0.202	0.069	0.202	0.069	-0.208	-0.336	-0.208	-0.336	-0.208	-0.336
CsB'_2X_3	-1.054	-0.983	-0.805	-0.817	-0.617	-0.639	-0.982	-0.980	-0.785	-0.858	-0.642	-0.708	-0.704	-0.693	-0.538	-0.595	-0.458	-0.507
$CsB'X_2$	-1.283	-1.178	-1.022	-1.008	-0.794	-0.796	-1.291	-1.241	-1.060	-1.094	-0.859	-0.901	-1.035	-0.969	-0.844	-0.864	-0.706	-0.731
$CsB'X_3$	-1.234	-1.137	-0.961	-0.955	-0.707	-0.709	-1.225	-1.108	-0.950	-0.926	-0.720	-0.722	-1.146	-1.066	-0.893	-0.904	-0.708	-0.721
CsX	-2.059	-1.983	-1.800	-1.805	-1.541	-1.561	-2.059	-1.983	-1.800	-1.805	-1.541	-1.561	-2.059	-1.983	-1.800	-1.805	-1.541	-1.561
CsX_3	-1.195	-1.081	-1.020	-0.991	-0.835	-0.841	-1.195	-1.081	-1.020	-0.991	-0.835	-0.841	-1.195	-1.081	-1.020	-0.991	-0.835	-0.841
CsX_4	-0.994	-0.874	-0.805	-0.807	-0.677	-0.683	-0.994	-0.874	-0.805	-0.807	-0.677	-0.683	-0.994	-0.874	-0.805	-0.807	-0.677	-0.683
$Cs_2BB'X_6$	-1.387	-1.272	-1.071	-1.055	-0.785	-0.780	-1.384	-1.308	-1.080	-1.095	-0.813	-0.827	-1.275	-1.191	-0.996	-1.002	-0.762	-0.766

Table 3: Quaternary Phase Diagram Analysis. Predicted decomposition reactions and the corresponding to the maximum decomposition energies calculated from the quaternary phase diagrams of each of the 18 pnictogen/halide double perovskites using DFT/LDA and DFT/PBE. The decomposition energy is defined as the difference between the total energy of the decomposition products and the total energy of the double perovskite. For unstable compounds, the decomposition energy is calculated as the energy separation from the convex hull, using the Pymatgen package. For the stable compounds the decomposition energies are calculated as described in the methods.

Compound	Predicted Decomposition Reaction		Decomposition		Conclusion	Experiment
	LDA	PBE	LDA	PBE		
$Cs_2BiCuCl_6$	$\frac{1}{2}$ $Cs_3Bi_2Cl_9$ + $\frac{1}{2}$ $CsCu_2Cl_3$	$\frac{1}{2}$ $Cs_3Bi_2Cl_9$ + $\frac{1}{2}$ $CsCu_2Cl_3$	19.1	-23.9	inconclusive	N/A
$Cs_2BiCuBr_6$	$\frac{1}{2}$ $Cs_3Bi_2Br_9$ + $\frac{1}{2}$ $CsCu_2Br_3$	$\frac{1}{2}$ $Cs_3Bi_2Br_9$ + $\frac{1}{2}$ $CsCu_2Br_3$	0.8	-30.7	not stable	N/A
Cs_2BiCuI_6	$\frac{1}{2}$ $Cs_3Bi_2I_9$ + $\frac{1}{2}$ $CsCu_2I_3$	$\frac{2}{3}$ CsI + $\frac{1}{2}$ $Cs_3Bi_2I_9$ + $\frac{1}{6}$ $Cs_3Cu_2I_5$	-31.5	-45.5	not stable	N/A
$Cs_2SbCuCl_6$	$\frac{1}{2}$ $Cs_3Sb_2Cl_9$ + $\frac{1}{2}$ $CsCu_2Cl_3$	$\frac{1}{2}$ $Cs_3Sb_2Cl_9$ + $\frac{1}{2}$ $CsCu_2Cl_3$	9.5	-35.0	inconclusive	N/A
$Cs_2SbCuBr_6$	$\frac{1}{2}$ $Cs_3Sb_2Br_9$ + $\frac{1}{2}$ $CsCu_2Br_3$	$\frac{1}{2}$ $Cs_3Sb_2Br_9$ + $\frac{1}{2}$ $CsCu_2Br_3$	-5.0	-37.4	not stable	N/A
Cs_2SbCuI_6	$\frac{1}{2}$ $Cs_3Sb_2I_9$ + $\frac{1}{2}$ $CsCu_2I_3$	$\frac{2}{3}$ CsI + $\frac{1}{2}$ $Cs_3Sb_2I_9$ + $\frac{1}{6}$ $Cs_3Cu_2I_5$	-29.4	-54.5	not stable	N/A
$Cs_2BiAgCl_6$	$\frac{1}{2}$ Ag + $Cs_3Bi_2Cl_9$ + $\frac{1}{2}$ $CsAgCl_3$	$\frac{1}{2}$ $Cs_3Bi_2Cl_9$ + $\frac{1}{2}$ $CsAg_2Cl_3$	24.5	12.1	stable	stable[27–29]
$Cs_2BiAgBr_6$	$\frac{1}{2}$ Ag + $\frac{1}{2}$ $Cs_3Bi_3Br_9$ + $\frac{1}{2}$ $CsAgBr_3$	$AgBr$ + $\frac{1}{3}$ $Cs_3Bi_2Br_9$ + $\frac{1}{3}$ Cs_3BiBr_6	16.5	-2.8	stable	stable[26,27,29]
Cs_2BiAgI_6	$\frac{1}{2}$ $Cs_3Bi_2I_9$ + $\frac{1}{2}$ $CsAg_2I_3$	$\frac{1}{2}$ $Cs_3Bi_2I_9$ + $\frac{1}{2}$ $CsAg_2I_3$	-5.6	-24.4	not stable	not stable
$Cs_2SbAgCl_6$	$\frac{1}{2}$ Ag + $\frac{1}{2}$ $Cs_3Sb_2Cl_9$ + $\frac{1}{2}$ $CsAgCl_3$	$\frac{1}{2}$ $Cs_3Sb_2Cl_9$ + $\frac{1}{2}$ $CsAg_2Cl_3$	16.5	1.9	stable	stable[33]
$Cs_2SbAgBr_6$	$\frac{1}{2}$ Ag + $\frac{1}{2}$ $Cs_3Sb_3Br_9$ + $\frac{1}{2}$ $CsAgBr_3$	$\frac{1}{2}$ $Cs_3Sb_2Br_9$ + $\frac{1}{2}$ $CsAg_2Br_3$	8.3	-9.6	inconclusive	not stable[36]
Cs_2SbAgI_6	$\frac{1}{2}$ $Cs_3Sb_2I_9$ + $\frac{1}{2}$ $CsAg_2I_3$	$\frac{1}{2}$ $Cs_3Sb_2I_9$ + $\frac{1}{2}$ $CsAg_2I_3$	-8.2	-26.4	not stable	N/A
$Cs_2BiAuCl_3$	$\frac{1}{2}$ Au + $\frac{1}{2}$ $Cs_2Bi_2Cl_9$ + $\frac{1}{2}$ $CsAuCl_3$	$\frac{1}{2}$ Au + $\frac{1}{2}$ $Cs_2Bi_2Cl_9$ + $\frac{1}{2}$ $CsAuCl_3$	-70.9	-82.4	not stable	N/A
$Cs_2BiAuBr_3$	$\frac{1}{2}$ Au + $\frac{1}{2}$ $Cs_2Bi_2Br_9$ + $\frac{1}{2}$ $CsAuBr_3$	$\frac{1}{2}$ Au + $\frac{1}{2}$ $Cs_2Bi_2Br_9$ + $\frac{1}{2}$ $CsAuBr_3$	-63.0	-54.0	not stable	N/A
Cs_2BiAuI_3	$\frac{1}{2}$ Au + $\frac{1}{2}$ $Cs_2Bi_2I_9$ + $\frac{1}{2}$ $CsAuI_3$	$\frac{1}{2}$ Au + $\frac{1}{2}$ $Cs_2Bi_2I_9$ + $\frac{1}{2}$ $CsAuI_3$	-53.9	-50.1	not stable	N/A
$Cs_2SbAuCl_3$	$\frac{1}{2}$ Au + $\frac{1}{2}$ $Cs_2Sb_2Cl_9$ + $\frac{1}{2}$ $CsAuCl_3$	$\frac{1}{2}$ Au + $\frac{1}{2}$ $Cs_2Sb_2Cl_9$ + $\frac{1}{2}$ $CsAuCl_3$	-72.5	-87.3	not stable	N/A
$Cs_2SbAuBr_3$	$\frac{1}{2}$ Au + $\frac{1}{2}$ $Cs_2Sb_2Br_9$ + $\frac{1}{2}$ $CsAuBr_3$	$\frac{1}{2}$ Au + $\frac{1}{2}$ $Cs_2Sb_2Br_9$ + $\frac{1}{2}$ $CsAuBr_3$	-61.6	-71.5	not stable	N/A
Cs_2SbAuI_3	$\frac{1}{2}$ Au + $\frac{1}{2}$ $Cs_2Sb_2I_9$ + $\frac{1}{2}$ $CsAuI_3$	$\frac{1}{2}$ Au + $\frac{1}{2}$ $Cs_2Sb_2I_9$ + $\frac{1}{2}$ $CsAuI_3$	-44.3	-55.4	not stable	N/A

Table 4: Calculated decomposition energies for all possible reactions in the pseudo-ternary phase diagrams of $Cs_2BiAgCl_6$, $Cs_2BiAgBr_6$, Cs_2BiAgI_6 and $Cs_2BiCuCl_6$. All energies are expressed in meV/atom. The bolded lines represent the decomposition reactions represented in Figure 5.

	$Cs_2BiAgCl_6$		$Cs_2BiAgBr_6$		Cs_2BiAgI_6		$Cs_2BiCuCl_6$	
Reaction	LDA	PBE	LDA	PBE	LDA	PBE	LDA	PBE
$2CsX + BX_3 + B'X$	98.1	100.5	84.3	41.9	38.2	1.2	93.3	71.1
$1/2\ CsX + 1/2\ Cs_3B_2X_9 + B'X$	39.5	21.7	33.6	3.9	4.9	-22.0	34.7	-7.7
$1/2\ Cs_3B_2X_9 + 1/2\ CsB'_2X_3$	35.1	12.1	18.6	-1.9	-5.6	-24.4	19.1	-23.9
$1/3\ BX_3 + B'X + 2/3\ Cs_3BX_6$	34.9	29.8	31.6	3.2	8.5	-16.9	30.1	0.4
$BX_3 + 1/2\ CsB'_2X_3 + 3/2\ CsX$	94.6	90.8	69.2	36.2	27.7	-1.2	77.7	54.8
$1/2\ BX_3 + 1/2\ CsB'_2X_3 + 1/2\ Cs_3BX_6$	47.3	37.9	29.8	7.2	5.4	-14.8	30.3	1.9
$BX_3 + CsB'X_2 + CsX$	78.9	86.4	60.9	36.3	30.7	6.9	86.8	76.9
$2/3\ BX_3 + CsB'X_2 + 1/3\ Cs_3BX_6$	47.3	51.1	34.6	17.0	15.8	-2.2	55.2	41.5
$1/3\ BX_3 + CsB'X_2 + 1/3\ Cs_3B_2X_9$	39.9	33.9	27.1	10.9	8.5	-8.6	47.7	24.3
$BX_3 + 1/2\ Cs_3B'_2X_5 + 1/2\ CsX$	86.6	91.3	62.3	37.9	20.4	0.8	65.5	42.3
$5/6\ BX_3 + 1/2\ Cs_3B'_2X_5 + 1/6\ Cs_3BX_6$	70.8	73.7	49.1	28.2	13.0	3.7	49.7	24.6
$2/3\ BX_3 + 1/2\ Cs_3B'_2X_5 + 1/6\ Cs_3B_2X_9$	67.1	65.1	45.4	25.2	9.3	-6.9	46.0	16.0
$BX_3 + CsB'_2X_3$	69.9	77.8	50.6	26.7	14.3	-6.5	67.3	58.9
$3/4\ B'X + 1/2\ Cs_3B_2X_9 + 1/4\ Cs_2B'X_3$	32.5	16.0	25.2	0.1	-1.1	-23.9	28.2	-10.8
$2/3\ B'X + 1/2\ Cs_3B_2X_9 + 1/6\ Cs_3B'_2X_5$	35.7	18.6	26.3	2.5	-1.0	-22.1	25.5	-17.3
$1/2\ B'X + 1.2\ Cs_3B_2X_9 + 1/2\ CsB'X_2$	29.9	14.7	21.9	1.1	1.1	-19.1	31.5	-4.8
$B'X + 1/3\ Cs_3B_2X_9 + 1/3\ Cs_3BX_6$	27.5	12.6	24.2	-2.8	1.1	-23.3	22.7	-16.8

Results

To establish which of the 18 proposed halide double perovskites are stable against decomposition, we construct the quaternary phase diagrams for each of the Cs - B - B′ - X systems (B = Bi, Sb, B′ = Cu, Ag, Au and X = Cl, Br, I). Visually, a quaternary phase diagram can be represented as a tetrahedron (Figure 1b), with the corners representing the elemental compounds, and all possible stable compositions being represented by nodes on the sides, faces, or inside the tetrahedron. Each node is connected with at least one other node by the so-called 'tie lines', which are not shown in Figure 1b for clarity.

In Figure 2 we show the largest energies of decomposition calculated from the quaternary phase diagrams of all 18 double perovskites. We first want to understand the sensitivity of our results to the choice of exchange correlation functional, by evaluating the decomposition

Table 5: Calculated decomposition energies for all possible reactions in the pseudo-ternary phase diagrams of $Cs_2SbAgCl_6$, $Cs_2SbAgBr_6$,$Cs_2SbCuCl_6$. All energies are expressed in meV/atom. The bolded lines represent the decomposition reactions plotted in Figure 5.

	$Cs_2SbAgCl_6$		$Cs_2SbAgBr_6$		$Cs_2SbCuCl_6$	
Reaction	LDA	PBE	LDA	PBE	LDA	PBE
$2CsX + BX_3 + B'X$	103.8	75.9	99.9	54.7	97.3	45.6
$1/2\ CsX + 1/2\ Cs_3B_2X_9 + B'X$	31.5	11.6	25.3	-3.9	25.1	-18.8
$1/2\ Cs_3B_2X_9 + 1/2\ CsB'_2X_3$	28.1	1.9	10.3	-9.6	9.5	-35.0
$1/3\ BX_3 + B'X + 2/3\ Cs_3BX_6$	43.8	26.8	42.5	12.3	37.4	-3.6
$BX_3 + 1/2\ CsB'_2X_3 + 3/2\ CsX$	100.3	66.3	84.8	49.0	81.7	29.4
$1/2\ BX_3 + 1/2\ CsB'_2X_3 + 1/2\ Cs_3BX_6$	55.4	29.5	41.8	17.2	36.8	-7.5
$BX_3 + CsB'X_2 + CsX$	84.6	61.9	76.5	49.1	90.8	51.4
$2/3\ BX_3 + CsB'X_2 + 1/3\ Cs_3BX_6$	54.6	37.3	47.8	27.9	60.9	26.8
$1/3\ BX_3 + CsB'X_2 + 1/3\ Cs_3B_2X_9$	36.4	19.0	26.8	10.0	42.7	8.5
$BX_3 + 1/2\ Cs_3B'_2X_5 + 1/2\ CsX$	92.3	66.8	77.9	50.7	59.6	16.8
$5/6\ BX_3 + 1/2\ Cs_3B'_2X_5 + 1/6\ Cs_3BX_6$	77.3	54.5	63.5	40.1	54.6	4.5
$2/3\ BX_3 + 1/2\ Cs_3B'_2X_5 + 1/6\ Cs_3B_2X_9$	68.2	45.3	53.0	31.2	45.5	-4.7
$BX_3 + CsB'_2X_3$	75.6	53.3	66.2	39.5	71.4	33.4
$3/4\ B'X + 1/2\ Cs_3B_2X_9 + 1/4\ Cs_2B'X_4$	24.5	5.9	16.9	-7.7	18.6	-21.8
$2/3\ B'X + 1/2\ Cs_3B_2X_9 + 1/6\ Cs_3B'_2X_5$	27.7	8.5	18.0	-5.3	15.9	-28.4
$1/2\ B'X + 1.2\ Cs_3B_2X_9 + 1/2\ CsB'X_2$	21.9	4.5	13.7	-6.7	21.9	-15.9
$B'X + 1/3\ Cs_3B_2X_9 + 1/3\ Cs_3BX_6$	25.6	8.5	21.5	-5.6	19.2	-21.9

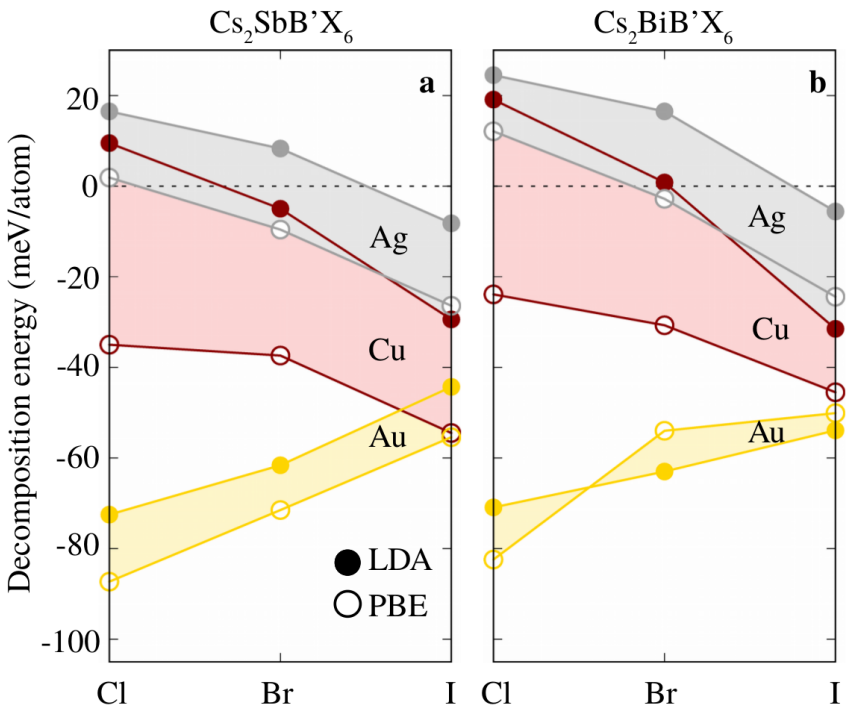

Figure 2: **Stability of the halide double perovskites**. Decomposition energies of each of the 18 halide double perovskites with respect to all possible decomposition routes (Sb-based perovskites in **a** and Bi-based perovskites in **b**). For the unstable perovskites, the decomposition energy is the energy above the convex hull, as calculated from Pymatgen. For the stable perovskites, the decomposition energy is calculated as the maximum decomposition energy obtained from all possible reaction pathways containing a maximum of four decomposition products, as described in the Methods. The filled/empty circles represent results obtained within LDA/PBE, respectively. All compounds containing Ag are in grey, Cu in dark red and Au in dark yellow. The shadings highlight the difference between the results obtained within LDA and PBE.

energies calculated within LDA and PBE. The energies of decomposition calculated for the same compound using the two functionals can differ by more than 40 meV/atom. Furthermore, from all calculations we can see that decomposition energies calculated within PBE are consistently larger than those obtained within LDA, with the difference decreasing as the size of the noble metal increases. The discrepancy between LDA and PBE decomposition energies is connected with the sensitivity of the formation energies to the exchange-correlation functional, and is well documented in literature.[64–67] Here we take into account this sensitivity by making the assumption that the decomposition energies calculated from LDA and PBE bracket the range of experimental decomposition energies, in the same spirit as in

Ref. 68. We also emphasize that we calculate phase diagrams at zero temperature and zero pressure, and the formation energies do not include the contribution from the zero-point motion. Therefore our calculations cannot be compared directly with experimental data of formation enthalpies, which are usually available at room temperature. However, since we are interested in identifying potential routes to synthesizing double perovskites with low gaps, we use the calculated phase diagrams to identify stability trends.

Several unambiguous trends can be identified from Figures 2a and b. (i) All Au-based hypothetical double perovskites are unstable, and will decompose into elemental Au, the perovskite $Cs_2Au^{(I)}Au^{(III)}X_6$, and $Cs_3B_2X_9$ (See Table 3). This decomposition reaction is due to the partial oxidation of Au^+ into Au^{3+}, leading to the preferential formation of the mixed-valency perovskite $Cs_2Au^{(I)}Au^{(III)}X_6$.[69] Given that both LDA and PBE point to the same decomposition route, and given the low decomposition energies obtained for all Au-based compounds (<-40 meV/atom), we conclude that all Au-based double perovskites are unstable. Accordingly, we do not explore these compounds any further in this manuscript. (ii) Cu-based double perovskites exhibit consistently lower decomposition energies than those calculated for the Ag compounds. This result is in agreement with recent theoretical and experimental work by Xiao et al.,[70] where the instability was attributed to the tendency of Cu^+ cations to arrange in a 4-fold coordination with the surrounding halogen anions. (iii) For the Cu- and Ag-based double perovskites we identify the same trend with respect to the halide composition, whereby the stability increases when moving from iodides to chlorides. This trend is consistent with the case of lead-halide perovskites, where the stability of $CsPbX_3$ and $CH_3NH_3PbX_3$ decreases from X = Cl, Br to I due to an increase in the ionization energy of the PbX_6 inorganic cage.[71]

In Table 3 we summarize the results of the analysis of the quaternary phase diagrams, alongside with available experimental information. Our calculations indicate that $Cs_2BiAgCl_6$, and $Cs_2SbAgCl_6$ are stable against decomposition, in agreement with experiment.[27,28,33]

For $Cs_2BiAgBr_6$ we obtain a positive decomposition energy in LDA, while PBE yields a marginally negative decomposition energy of -2.8 meV/atom. This value falls within the estimated sensitivity of our total energy calculations (as discussed in the Methods), and therefore we assign $Cs_2BiAgBr_6$ as stable in Table 3. Furthermore, our calculations correctly show that Cs_2BiAgI_6 does not form, and that the $Cs_3Bi_2I_9$ biproduct is obtained instead (see Table 3). This finding is in agreement with unsuccessful synthesis attempts made by our collaborators. Due to the large variation in the decomposition energies between LDA and PBE, our results are inconclusive for the following three cases: $Cs_2SbCuCl_6$, $Cs_2BiCuCl_6$ and $Cs_2SbAgBr_6$.

To be able to understand whether it is possible to stabilize mixed halide and mixed-noble metal double perovskites, we first take a closer look at the typical synthesis reaction for the pure compounds, shown in Eq. 1. We can study these reactions in more detail from *ab initio* calculations by constructing pseudo-ternary phase diagrams for each of the systems considered, in such a way that the corners of the triangles are the precursor reactants (see Figure 3). Visually, this pseudo-ternary diagram can be understood as a 'slice' through the quaternary phase diagram along the plane defined by the three precursors, as shown in Figure 1b. In doing so, we only analyze the decomposition routes that involve compounds belonging to this plane. The decomposition routes competing with the formation of the double perovskite can be read on the new pseudo-ternary phase diagrams by identifying all segments passing through the node corresponding to the double perovskite, or all triangles surrounding it. For each of the double perovskites there are 17 possible decomposition routes, summarized in the first column of Tables 4 and 5.

In Figures 3 and 4 we show the pseudo ternary phase diagrams thus constructed, as calculated within the LDA and PBE, respectively. On each ternary phase diagram in Figures 3 and 4 we overlay the formation energy of each composition with respect to the precursors at the corners of the diagram. In all diagrams, the formation of the double perovskite appears to

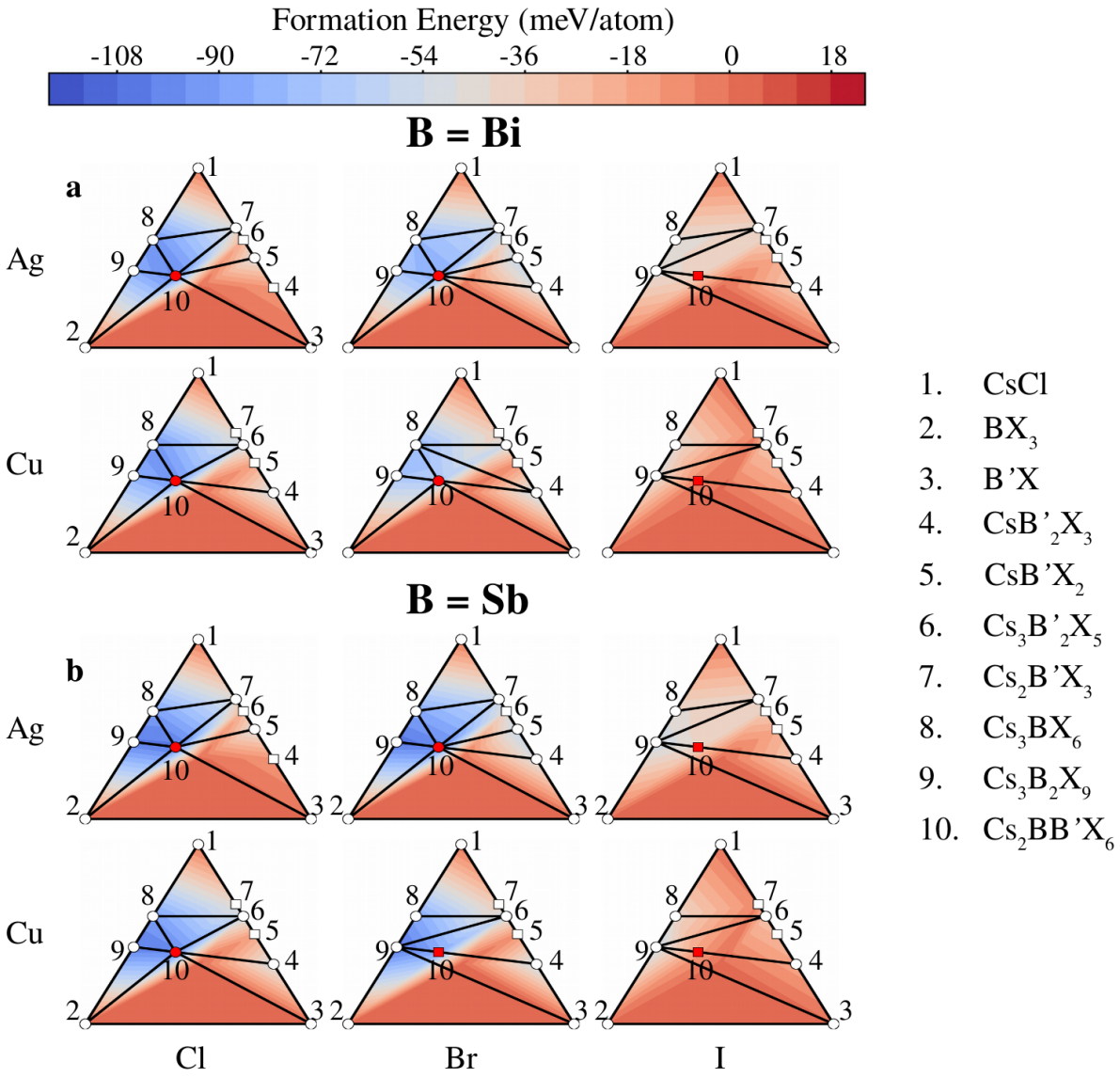

Figure 3: **Pseudo-ternary phase diagrams of halide double perovskites.** Ternary phase diagrams of halide double perovskites obtained by slicing the quaternary phase diagram with a plane corresponding to the precursors used in solid-state synthesis. The corners of the triangles are CsX (X = Cl, Br, I), BX_3 [B = Bi(**a**), Sb (**b**) and X = Cl, Br, I] and B′X (B' = Cu, Ag and X = Cl, Br, I). The colour maps represent the formation energy at each point of the phase diagram with respect to its corners (obtained from interpolation through the vertices). The white disks and squares on the diagram correspond to the stable and unstable compounds, respectively, and the red disks and squares correspond to the stable and unstable double perovskites, respectively. The position of the points in the diagram reflect the number of atoms for corresponding compounds in the balanced reactions. The phase diagrams were constructed using the total energies calculated from LDA. 4.

be in competition with the formation of $Cs_3Bi_2X_9$ or $Cs_3Sb_2X_9$, and $CsAg_2X_3$ or $CsCu_2X_3$.

In the case of $Cs_2BiAgCl_6$, $Cs_2BiAgBr_6$ and $Cs_2SbAgCl_6$ the formation energy of the double

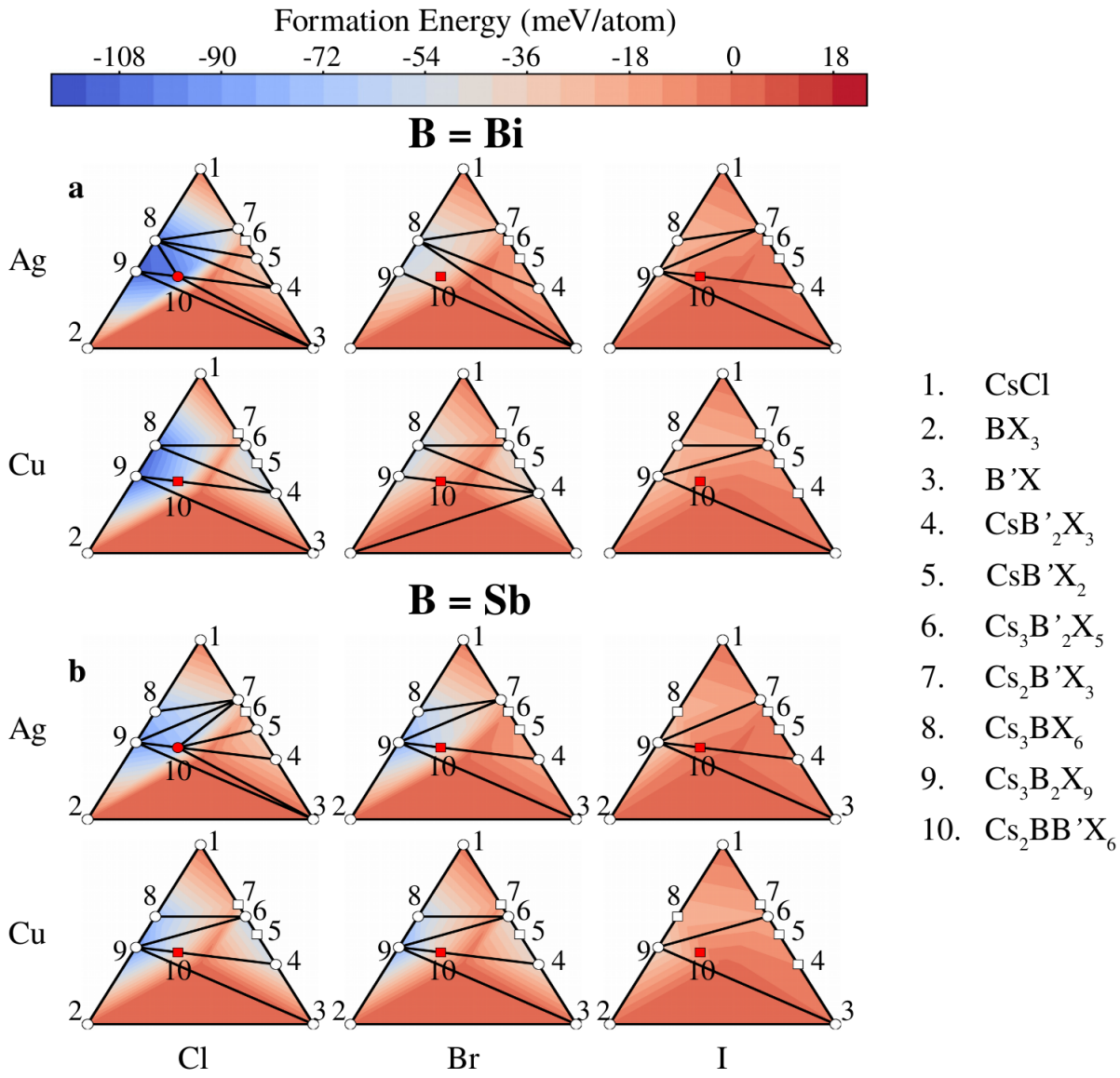

Figure 4: **Pseudo-ternary phase diagrams of halide double perovskites.** Ternary phase diagrams of halide double perovskites obtained by slicing the quaternary phase diagram with a plane corresponding to the precursors used in solid-state synthesis. The corners of the triangles are CsX (X = Cl, Br, I), BX_3 [B = Bi(**a**), Sb (**b**) and X = Cl, Br, I] and B′X (B' = Cu, Ag and X = Cl, Br, I). The colour maps represent the formation energy at each point of the phase diagram with respect to its corners (obtained from interpolation through the vertices). The white disks and squares on the diagram correspond to the stable and unstable compounds, respectively, and the red disks and squares correspond to the stable and unstable double perovskites, respectively. The position of the points in the diagram reflect the number of atoms for corresponding compounds in the balanced reactions. The phase diagrams were constructed using the total energies calculated from PBE.

perovskite is slightly larger than the energy of $Cs_3Bi_2Cl_9$, $Cs_3Bi_2Br_9$ and $Cs_2Sb_2Cl_9$, and much smaller than that of the corresponding silver halides $CsAg_2X_3$, therefore the double

perovskite sits on the convex hull. However, by moving towards iodine, the formation energy of the double perovskite increases, lifting the correspoding node above the convex hull, favouring instead the formation of $Cs_3Bi_2X_9$ or $Cs_3Sb_2X_9$ and $CsAg_2X_3$ or $CsCu_2X_3$.

This analysis suggests that it should be possible to suppress the formation of the competing ternary compounds ($Cs_3Bi_2X_9$, $Cs_3Sb_2X_9$, $CsAg'_2X_3$ and $CsCu_2X_3$), by mixing I, Br, or Cu into the already known stable double perovskites ($Cs_2BiAgCl_6$, $Cs_2BiAgBr_6$ and $Cs_2SbAgCl_6$), so as to form the following possible mixed perovskites: $Cs_2BiAg_{1-x}Cu_xCl_6$, $Cs_2SbAg_{1-x}Cu_xCl_6$, $Cs_2BiAg(Br_{1-x}I_x)_6$, and $Cs_2BiAg(Cl_{1-x}Br_x)_6$. We first explore this idea qualitatively, by examining the decomposition energies of $Cs_2BiAgCl_6$, $Cs_2BiAgBr_6$, Cs_2BiAgI_6, $Cs_2BiCuCl_6$, $Cs_2SbAgCl_6$, $Cs_2SbAgBr_6$, and $Cs_2SbCuCl_6$ with respect to all 17 possible decomposition routes. These energies are listed in Table 4 and 5.

In a first approximation we evaluate the decomposition energy of a mixed double perovskite of the type $Cs_2BAg(X_{1-x}Y_{1-y})_6$ or $Cs_2BAg_{1-x}Cu_xX_6$ (B = Bi, Sb, X = Cl, Br and Y = Br, I) using a linear interpolation between the pure compounds. In Figures 5a-d we plot the decomposition energies thus calculated for $Cs_2BiAg_{1-x}Cu_xCl_6$, $Cs_2SbAg_{1-x}Cu_xCl_6$, $Cs_2BiAg(Br_{1-x}I_x)_6$, and $Cs_2BiAg(Cl_{1-x}Br_x)_6$. Thin lines correspond to the linear combinations of the decomposition energies for the same reaction pathway, both in LDA and PBE . The thick lines correspond to the lowest decomposition energies at each concentration. In the case of $Cs_2BiAg_{1-x}Cu_xCl_6$, decomposition energies calculated from both LDA and PBE are positive for a concentration of Cu up to 30%. By contrast, in the case of $Cs_2SbAg_{1-x}Cu_xCl_6$, $Cs_2BiAg(Br_{1-x}I_x)_6$, $Cs_2BiAg(Cl_{1-x}Br_x)_6$, the decomposition energies from LDA and PBE have opposite signs for almost the entire range of concentrations, and are therefore inconclusive. For this reason we now focus only on the unambiguous case of $Cs_2BiAg_{1-x}Cu_xCl_6$.

To investigate in more detail if $Cs_2BiAg_{1-x}Cu_xCl_6$ is likely to form, we construct two ordered mixed double perovskites with 12.5% and 25% Cu, as described in the Methods,

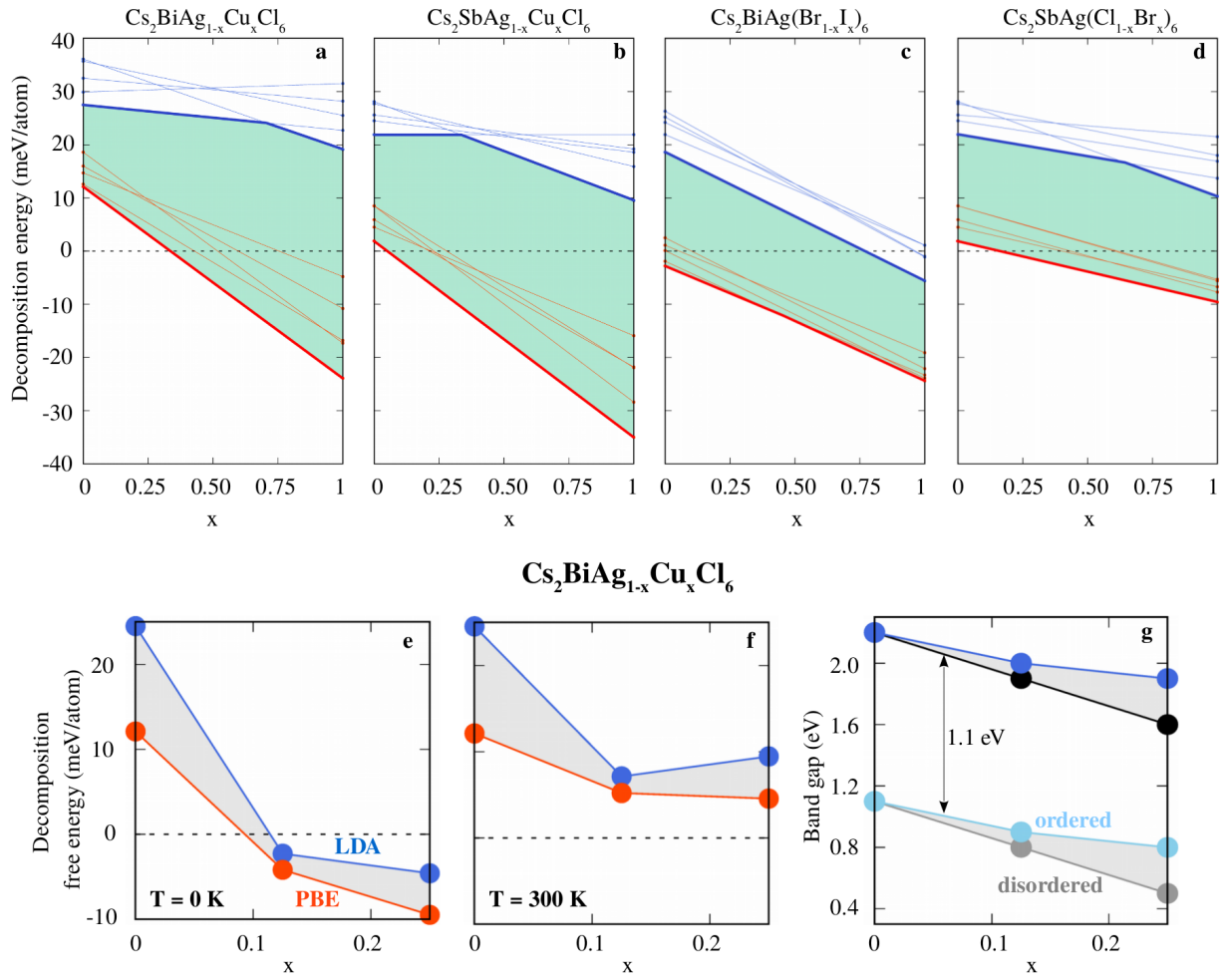

Figure 5: **Stability and band gaps of mixed halide and mixed-noble metal double perovskites. a-d** Decomposition energy of mixed double perovskites $Cs_2BiAg_xCu_{1-x}Cl_6$ (**a**), $Cs_2SbAg_{1-x}Cu_xCl_6$ (**b**), $Cs_2BiAg(Br_{1-x}I_x)_6$ (**c**) and $Cs_2SbAg(Cl_{1-x}Br_x)_6$ (**d**). The decomposition energies corresponding to the endpoints of the thin lines are calculated with respect to reaction pathways with the five lowest decomposition energies (highlighted in bold in Tables 4 and 5). The lines connect the decomposition energies calculated from the same reaction pathway. The thick lines correspond to the the decomposition pathways that yield the lowest decomposition energies. The green shading highlights the region of stability. Lowest decomposition free energy calculated from the five-element convex hull at 0 K (**e**) and 300 K (**f**) of the ordered mixed double perovskites. The red and blue dots are direct calculations. At $T = 300$ K, we include the contribution of the ideal mixing entropy, as discussed in the main text. **g** Band gap of the mixed double perovskite $Cs_2BiAg_{1-x}Cu_xCl_6$ for different concetrations of Cu. The light-blue and grey dots represent calculations on the ordered and the disordered mixes, respectively. The darker dots are the band gaps blue-shifted by 1.1 eV (blue and black dots, respectively). This value is chosen so that the band gap of $Cs_2BiAgCl_6$ matches the experimental band gap reported in Refs. 28,29. All band gaps are calculated within DFT/LDA, and the calculations on the disordered structure are performed within the virtual crystal approximation.

and we calculate their total energies within LDA and PBE. From the analysis of the five-element convex hull, Cs-Bi-Ag-Cu-Cl, we obtain that both mixed compounds are marginally unstable, with the lowest decomposition energies between −2.3 meV/atom (LDA) and −4.2 meV/atom (PBE) for $Cs_2BiAg_{0.875}Cu_{0.125}Cl_6$ and between −4.6 meV/atom (LDA) and −9.5 meV/atom (PBE) for $Cs_2BiAg_{0.75}Cu_{0.25}Cl_6$, as shown in Figure 5e. According to the convex hull, both compounds are expected decompose into either $Cs_2BiAg_{1-x}Cu_xCl_6 \rightarrow (1-x)\ Cs_2BiAgCl_6 + x\ Cs_2BiCuCl_6$ (as predicted by LDA) or $Cs_2BiAg_{1-x}Cu_xCl_6 \rightarrow (1-x)\ Cs_2BiAgCl_6 + x/2\ Cs_3Bi_2Cl_9 + x/2\ CsCu_2Cl_3$ (as predicted by PBE). However, considering that these calculations are performed on ordered structures at 0 K, and that the calculated energies above the hull are very small, it is likely that entropic effects at higher temperatures will stabilize $Cs_2BiAg_{1-x}Cu_xCl_6$ mixes. This possibility has recently been demonstrated experimentally in Ref. 72, where disordered mixed oxides were stabilized by the mixing entropy.

A rigorous theoretical treatment of the mixing entropy for $Cs_2BiAg_{1-x}Cu_xCl_6$ would require the calculations on very large supercells, in order to fully account for disorder[73] or an analysis within the special quasi-random structures[74] or the cluster expansion approaches,[75] which would go beyond the scope of this study. Instead, we evaluate the magnitude of the entropic effects by considering the ideal mixing entropy, $S_{\mathrm{mix}} = -k_{\mathrm{B}}[x \log x + (1-x) \log (1-x)]$, where x is the mixing concentration and k_{B} is the Boltzmann constant, in a similar approach as in Ref. 76. In Figure 5 we plot the free energy of decomposition $\Delta F = \Delta E_{\mathrm{tot}} + TS_{\mathrm{mix}}$, at $T = 300$ K for the $Cs_2BiAg_{1-x}Cu_xCl_6$ series. Within this approximate treatment, we show that it should be possible to form $Cs_2BiAg_{1-x}Cu_xCl_6$ by using the entropy of mixing as a control parameter.

Finally, we evaluate whether exploring the $Cs_2BiAg_{1-x}Cu_xCl_6$ mixed perovskites is likely to improve the performance of lead-free double perovskite solar cells, by calculating the dependence of the band gap on the concentration of Cu. In Figure 5g we show the band gaps of the

$Cs_2BiAg_{1-x}Cu_xCl_6$ calculated either within the virtual crystal approximation[63] or using the ordered structures of $Cs_2BiAg_{0.75}Cu_{0.25}Cl_6$ and $Cs_2BiAg_{0.875}Cu_{0.125}Cl_6$ from DFT/LDA, including spin-orbit coupling. This approach is expected to underestimate the band gaps with respect to experiment by more than 1 eV. PBE0 hybrid functional calculations are known to overestimate the band gaps of these compounds by approximately 0.5 eV,[28] while the *GW* band gaps of $Cs_2BiAgCl_6$ and $Cs_2BiAgBr_6$ are in very good agreement with experiment.[29] Most importantly, the band gap trends identified at the DFT/LDA level remain consistent regardless of the level of theory employed. Therefore, in order to illustrate the dependence of the band gap on the concentration of Cu, in Figure 5g, we apply a rigid correction of 1.1 eV to all calculated DFT/LDA band gaps, so that the band gap of $Cs_2BiAgCl_6$ matches experiment. As shown in Figure 5g, increasing the concentrations of Cu up to 25%, leads to a reduction in the band gap to values between 1.6-1.9 eV. Based on these results, we propose that $Cs_2BiAg_{1-x}Cu_xCl_6$ series constitute a promising route to achieve pnictogen/noble metal double perovskites with reduced band gaps.

Conclusion

In summary, we investigated the thermodynamic stability of 18 hypothetical lead-free double perovskites of the type $Cs_2BB'X_6$, with B = Bi, Sb, B′ = Cu, Ag, Au and X = Cl, Br, I, using quaternary phase diagrams. Remarkably, we found that the three double perovskites of this family that have been synthesized so far are in fact the only stable double perovskites predicted by our calculations. Furthermore, we investigated the stability of solid solutions, and identified that the mixed $Cs_2BiAg_{1-x}Cu_xCl_6$ can be likely stabilized, and is a promising candidate for a mixed noble-metal halide double peroskite with reduced band gaps. One of the important observations of our study is that the decomposition energies calculated within density functional theory can vary by up to 40 meV/atom for this family of compounds, depending on the chosen approximation for the exchange-correlation functional. This ob-

servation calls for a careful interpretation of the phase diagrams calculated within DFT. We hope that our results will stimulate further experimental work on the synthesis and characterization of mixed-noble metal halide perovskites with tunable band gaps.

Acknowledgement

The research leading to these results has received funding from the the Graphene Flagship (Horizon 2020 Grant No. 696656 - GrapheneCore1 grant no. 604391), the Leverhulme Trust (Grant RL-2012-001), the UK Engineering and Physical Sciences Research Council (Grant No. M0205171/1). The authors would like to acknowledge the use of the University of Oxford Advanced Research Computing (ARC) facility.[77] The authors would like to acknowledge Amir Abbas Haghighirad for discussing synthesis attempts for Cs_2BiAgI_6 and George Volonakis for sharing the modified Quantum Espresso source code for the virtual crystal calculations.

References

(1) Kojima, A.; Teshima, K.; Shirai, Y.; T., M. Organometal Halide Perovskites as Visible-Light Sensitizers for Photovoltaic Cells. *J. Am. Chem. Soc.* **2009**, *131*, 6050.

(2) Best Research-Cell Efficiencies. `http://www.nrel.gov/ncpv/images/efficiency_chart.jpg`.

(3) McMeekin, D. P.; Sadoughi, G.; Rehman, W.; Eperon, G. E.; Saliba, M.; Höratner, M. T.; Haghighirad, A.; Sakai, N.; Korte, L.; Rech, B. et al. A Mixed-Cation Lead Mixed-Halide Perovskite Absorber for Tandem Solar Cells. *Science* **2016**, *351*, 151–155.

(4) Filip, M. R.; Eperon, G. E.; Snaith, H. J.; Giustino, F. Steric Engineering of Metal-Halide Perovskites with Tunable Optical Band Gaps. *Nat. Commun.* **2014**, *5*, 5757.

(5) Filip, M. R.; Verdi, C.; Giustino, F. *GW* Band Structure and Carrier Effective Mases of $CH_3NH_3PbI_3$ and Hypothetical Perovskites of the Type $APbI_3$: A = NH_4, PH_4, AsH_4 and SbH_4. *J. Phys. Chem. C* **2015**, *119*, 24209–24219.

(6) Miyata, A.; Mitioglu, A.; Plochocka, P.; Portugall, O.; Wang, J. T.-W.; Stranks, S. D.; Snaith, H. J.; Nicholas, R. J. Direct Measurement of the Exciton Binding Energy and Effective Masses for Charge Carriers in an Organic-Inorganic Tri-Halide Perovskite. *Nat. Phys.* **2015**, *11*, 582–587.

(7) Herz, L. M. Charge-Carrier Dynamics in Organic-Inorganic Metal Halide Perovskites. *Annu. Rev. Phys. Chem.* **2016**, *67*, 3.1–3.25.

(8) Saliba, M.; Matsui, T.; Domanski, K.; Seo, J.-Y.; Ummadisingu, A.; Zakeeruddin, S. M.; Correa-Baena, J.-P.; Tress, W. R.; Abate, A.; Hagfeldt, A. et al. Incorporation of Rubidium Cations into Perovskite Solar Cells Improves Photovoltaic Performance. *Science* **2016**,

(9) Eperon, G. E.; Leijtens, T.; Bush, K. A.; Prasanna, R.; Green, T.; Wang, J. T.-W.; McMeekin, D. P.; Volonakins, G.; Milot, R. L.; May, R. et al. Perovskite-perovskite tandem photovoltaics with optimized band gaps. *Science* **2016**, *354*, 861–865.

(10) Babagayigit, A.; Thanh, D. D.; Ethirajan, A.; Manca, J.; Muller, M.; Boyen, H.-G.; Conings, B. Assessing the Toxicity of Pb- and Sn-Based Perovskite Solar Cells in Model Organism Danio Rerio. *Sci. Rep.* **2016**, *6*, 18721.

(11) Pellet, N.; Gao, P.; Gregori, G.; Yang, T.-Y.; Nazeerrudin, M. K.; Maier, J.; Grätzel, M. Mixed-Organic-Cationic Perovskite Photovoltaics for Enhanced Solar-Light Harvesting. *Angew. Chem.* **2014**, *53*, 3151.

(12) Eperon, G. E.; Stranks, S. D.; Menelaou, C.; Johnston, M. B.; Herz, L. M.; Snaith, H. J. Formamidinium Lead Trihalide: A Broadly Tunable Perovskite for Efficient Planar Heterojunction Solar Cells. *Energ. Environ. Sci.* **2014**, *7*, 982–988.

(13) Noel, N.; Stranks, S. D.; Abate, A.; Wehrenfennig, C.; Guarnera, S.; Haghighirad, A.-A.; Sadhanala, A.; Eperon, G. E.; Pathak, S. K.; Johnston, M. B. et al. Lead-Free Organic-Inorganic Tin Halide Perovskite for Photovoltaic Applications. *Energ. Environ. Sci* **2014**, *7*, 3061.

(14) Hao, F.; Stoumpos, C. C.; Chang, R. P. H.; Kanatzidis, M. G. Anomalous Band Gap Behavior in Mixed Sn and Pb Perovskites Enables Broadening of Absorption Spectrum in Solar Cells. *J. Am . Chem. Soc.* **2014**, *136*, 8094–8099.

(15) Giustino, F.; Snaith, H. J. Toward Lead-Free Perovskite Solar Cells. *ACS Energy Letters* **2016**, *1*, 1233–1240.

(16) Park, B.-W.; Philippe, B.; Zhang, X.; Rensmo, H.; Boschloo, G.; Johansson, E. M. J. Bismuth Based Hybrid Perovskites $A_3Bi_2I_9$ (A: Methylammonium or Cesium) for Solar Cell Application. *Adv. Mater.* **2015**, *27*, 6806–6813.

(17) Saparov, B.; Hong, F.; Sun, J.-P.; Duan, H.-S.; Meng, W.; Cameron, S.; Hill, I. G.; Yan, Y.; Mitzi, D. B. Thin-Film Preparation and Characterization of $Cs_3Sb_2I_9$: A Lead-Free Layered Perovskite Semiconductor. *Chem. Mater.* **2015**, *27*, 5622–5632.

(18) Lee, B.; Stoumpos, C. C.; Zhou, N.; Hao, F.; Malliakas, C.; C.-Y., Y.; Marks, T. J.; Kanatzidis, M. G.; Chang, R. P. H. Air-Stable Molecular Semiconducting Iodosalts for Solar Cell Applications: Cs2SnI6 as a Hole Conductor. *J. Am. Chem. Soc.* **2014**, *136*, 15379–15385.

(19) Saparov, B.; Sun, J.-P.; Meng, W.; Xiao, Z.; Duan, H.-S.; Gunawan, O.; Shin, D.; Hill, I. G.; Yan, Y.; Mitzi, D. B. Thin-Film Deposition and Characterization of a Sn-Deficient Perovskite Derivative Cs_2SnI_6. *Chem. Mater.* **2016**, *28*, 2315–2322.

(20) Sakai, N.; Haghighirad, A. A.; Filip, M. R.; Nayak, P. K.; Nayak, S.; Ramadan, A.; Wang, Z.; Giustino, F.; Snaith, H. J. Solution-Processed Cesium Hexabromopalladate(IV), Cs_2PdBr_6, for Optoelectronic Applications. *J. Am. Chem. Soc.* **2017**, *139*, 6030–6033.

(21) Filip, M. R.; Giustino, F. Computational Screening of Homovalent Lead Substitution in OrganicInorganic Halide Perovskites. *J. Phys. Chem. C* **2016**, *120*, 166–173.

(22) Körbel, S.; Marques, M. A.; Botti, S. Stability and Electronic Properties of New Inorganic Perovskites from High-Throughput Ab Initio Calculations. *J. Mater. Chem. C* **2016**, *4*, 3157–3167.

(23) Jacobsson, T. J.; Pazoki, M.; Hagfeldt, A.; Edvinsson, T. Goldschmidts Rules and Strontium Replacement in Lead Halogen Perovskite Solar Cells: Theory and Preliminary Experiments on $CH_3NH_3SrI_3$. *J. Phys. Chem. C* **2015**, *119*, 25673–25683.

(24) Kumar, A.; Balasubramaniam, K. R.; Kangasabanik, J.; Alam, V.; Alam, A. Crystal structure, stability, and optoelectronic properties of the organic-inorganic wide-band-gap perovskite $CH_3NH_3BaI_3$: Candidate for transparent conductor applications. *Phys. Rev. B* **2016**, 180104.

(25) Lindsey, A.; McAlexander, W.; Stand, L.; Wu, Y.; Zhuravleva, M.; Melcher, C. L. Crystal Growth and Spectroscopic Performance of Large Crystalline Boules of $CsCaI_3$:Eu Scintillator. *J. Cryst. Growth* **2015**, *427*, 42–47.

(26) Slavney, A. H.; Hu, T.; Lindenberg, A. M.; Karunadasa, H. I. A Bismuth-Halide Double Perovskite with Long Carrier Recombination Lifetime for Photovoltaic Applications. *J. Am. Chem. Soc.* **2016**, *138*, 2138–2141.

(27) McClure, E. T.; Ball, M. R.; Windl, W.; Woodward, P. M. Cs2AgBiX6 (X = Br, Cl) New visible light absorbing, lead-free halide perovskite semiconductors. *Chem. Mater.* **2016**, *28*, 1348–1354.

(28) Volonakis, G.; Filip, M. R.; Haghighirad, A. A.; Sakai, N.; Wenger, B.; Snaith, H. J.; Giustino, F. Lead-free halide double perovskites via heterovalent substitution of noble metals. *J. Phys. Chem. Lett.* **2016**, *7*, 1254–1259.

(29) Filip, M. R.; Hillman, S.; Haghighirad, A. A.; Snaith, H. J.; Giustino, F. Band Gaps of the Lead-Free Halide Double Perovskites $Cs_2BiAgCl_6$ and $Cs_2BiAgBr_6$ from Theory and Experiment. *J. Phys. Chem. Lett.* **2016**, *7*, 2579–2585.

(30) Wei, F.; Deng, Z.; Sun, S.; Xie, F.; Kieslisch, G.; Evans, D. M.; Carpenter, M. A.; Bristowe, P. D.; Cheetham, A. K. The Synthesis, Structure and Electronic Properties of a Lead-Free Hybrid Inorganic-Organic Double Perovskite $(MA)_2KBiCl_6$ (MA = Methylammonium). *Mater. Horiz.* **2016**, *3*, 328–332.

(31) Deng, Z.; Wei, F.; Sun, S.; Kieslich, G.; Cheetham, A. K.; Bristowe, P. D. Exploring the Properties of Lead-Free Hybrid Double Perovskites using a Combined Computational-Experimental Approach. *J. Mater. Chem. A* **2016**, *4*, 1025–12029.

(32) Volonakis, G.; Haghighirad, A. A.; Milot, R. L.; Sio, W. H.; Filip, M. R.; Wenger, B.; Johston, M. B.; Herz, L. M.; Snaith, H. J.; Giustino, F. $Cs_2InAgCl_6$: A new lead-free halide double perovskite with direct band gap. *J. Phys. Chem. Lett.* **2017**, *8*, 772–778.

(33) Tran, T. T.; Panella, J. R.; Chamorro, J. R.; Morey, J. R.; McQueen, T. M. Designing Indirect-Direct Bandgap Transitions in Double Perovskites. *Mater. Horiz.* **2017**, *4*, 688.

(34) Wei, F.; Deng, Z.; Sun, S.; Zhang, F.; Evans, D. M.; Kieslich, G.; Tominaka, S.; Carpenter, M. A.; Zhang, J.; Bristowe, P. D. et al. Synthesis and Properties of a Lead-Free Hybrid Double Perovskite: $(CH_3NH_3)_2AgBiBr_6$. *Chem. Mater.* **2017**, *29*, 1089–1094.

(35) Slavney, A. H.; Leppert, L.; Bartesaghi, D.; Gold-Parker, A.; Toney, M. F.; Savenije, T. J.; Neaton, J. B.; Karunadasa, H. I. Defect-Induced Band-Edge Recon-

struction of a Bismuth-Halide Double Perovskite for Visible-Light Absorption. *J. Am. Chem. Soc.* **2017**, *139*, 5015–5018.

(36) Du, K.; Meng, W.; Wang, X.; Yan, Y.; Mitzi, D. B. Bandgap Engineering of Lead-Free Double Perovskite $Cs_2AgBiBr_6$ through Trivalent Metal Alloying. *Angew. Chem. Int. Ed.* **2017**, *56*, 8158.

(37) Zhao, X.-G.; Yang, D.; Sun, Y.; Li, T.; Zhang, L.; Yu, L.; Zunger, A. Cu-In Halide Perovskite Solar Absorbers. *J. Am. Chem. Soc.* **2017**, *139*.

(38) Volonakis, G.; Haghighirad, A. A.; Snaith, H. J.; Giustino, F. Route to Stable Lead-Free Double Perovskites with the Electronic Structure of $CH_3NH_3PbI_3$: A Case for Mixed-Cation $[Cs/CH_3NH_3/CH(NH_2)_2]_2InBiBr_6$. *J. Phys. Chem. Lett.* **2017**, *8*, 3917–3924.

(39) Zhao, X. G.; Yang, J.-H.; Fu, Y.; Yang, D.; Xu, Q.; Yu, L.; Wei, S.-H. Z. L. Design of Lead-Free Inorganic Halide Perovskites for Solar Cells via Cation-Transmutation. *J. Am. Chem. Soc.* **2017**, *139*, 2630–2638.

(40) Jain, A.; Voznyy, O.; Sargent, E. H. High-Throughput Screening of Lead-Free Perovskite-like Materials for Optoelectronic Applications. *J. Phys. Chem. C* **2017**, *121*, 7183–7187.

(41) Nakajima, T.; Sawada, K. Discovery of Pb-Free Perovskite Solar Cells via High-Throughput Simulation on the K Computer. *J. Phys. Chem. Lett.* **2017**, *8*, 4826–4831.

(42) Giorgi, G.; Yamashita, K. Alternative, Lead-Free, Hybrid Organic-Inorganic Perovskites for Solar Applications: A DFT Analysis. *Chem. Lett.* **2015**, *44*, 826.

(43) Xiao, Z.; Du, K.-Z.; Meng, W.; Wang, J.; Mitzi, D. B.; Yan, Y. Intrinsic Instability of $Cs_2In^{(I)}M^{(III)}X_6$ (M = Bi, Sb; X = Halogen) Double Perovskites: A Combined Density Functional Theory and Experimental Study. *J. Am. Chem. Soc.* **2017**, *139*, 6054–6057.

(44) Xiao, Z.; Meng, W.; Wang, J.; Yan, Y. Thermodynamic Stability and Defect Chemistry of Bismuth-Based Lead-Free Double Perovskites. *Chem. Sus. Chem.* **2016**, *9*, 2628–2633.

(45) Pan, W.; Wu, H.; Luo, J.; Deng, Z.; Ge, C.; Chen, C.; Jiang, X.; Yin, W.; Niu, G.; Zhu, L. et al. $Cs_2AgBiBr_6$ Single-Crystal X-Ray Detectors with a Low Detection Limit. *Nat. Photon.* **2017**,

(46) Greul, E.; Petrus, M. L.; Binek, A.; Docampo, P.; Bein, T. Highly Stable, Phase Pure $Cs_2AgBiBr_6$ Double Perovskite Thin Films for Optoelectronic Applications. *J. Mater. Chem. A* **2017**, *5*, 19972–19981.

(47) Shockley, W.; Queisser, H. J. Detailed Balance Limit of Efficiency of p-n Junction Solar Cells. *J. Appl. Phys.* **1961**, *32*, 510.

(48) Hohenberg, P.; Kohn, W. Inhomogeneous Electron Gas. *Phys. Rev.* **1964**, *136*, B864.

(49) Ong, S. P.; Wang, L.; Kang, B.; Ceder, G. Li-Fe-P-O2 Phase Diagram from First Principles Calculations. *Chem. Mater.* **2008**, *20*, 1798–1807.

(50) Ong, S. P.; Jain, G., A. Hautier; Kang, B.; Ceder, G. Thermal Stabilities of Delithiated Olivine MPO_4 (M = Fe, Mn) Cathodes Investigated Using First Principles Calculations. *Electrochem. Commun.* **2010**, *12*, 427–430.

(51) Emery, A. A.; Saal, J. E.; Kirklin, S.; Hedge, V. I.; Wolverton, C. High-throughput computational screening of perovskites for thermochemical water splitting applications. *Chem. Mater.* **2016**, *28*, 5621–5634.

(52) Yan, Q.; Yu, J.; Suram, S. K.; Zhou, L.; Shinde, A.; Newhouse, P. F.; Chen, W.; Li, G.; Persson, K. A.; Gregoire, J. M. et al. Solar fuels photoanode materials discovery by integrating high-throughput theory and experiment. *Proc. Nat. Acad. Sci.* **2016**, *114*, 3040–3043.

(53) Gianozzi, P.; Baroni, S.; Bonini, N.; Calandra, M.; Car, R.; Cavazzoni, C.; Ceresoli, D.; Chiarotti, G. L.; Cococcioni, M.; Dabo, I. et al. QUANTUM ESPRESSO: A Modular and Open-Source Software Project for Quantum Simulations of Materials. *J. Phys.: Condens. Matter.* **2009**, *21*.

(54) Perdew, J. P.; Zunger, A. Self-Interaction Correction to Density-Functional Approximations for Many-Electrons Systems. *Phys. Rev. B* **1981**, *23*, 5048.

(55) Perdew, J. P.; Burke, K.; Erzerhof, M. Generalized Gradient Approximation Made Simple. *Phys. Rev. Lett.* **1996**, *77*, 3865.

(56) Pseudopotentials. `http://theossrv1.epfl.ch/Main/Pseudopotentials`, accessed: September, 2015.

(57) Jain, A.; Ong, S. P.; Hautier, G.; Chen, W.; Richards, W. D.; Dacek, S.; Cholia, S.; Gunter, D.; Skinner, D.; Ceder, G. et al. The Materials Project: A Materials Genome Approach to Accelerating Materials innovation. *Adv. Phys. Lett. Materials* **2012**, *1*, 011002.

(58) Ong, S. P.; Richardson, W. D.; Jain, A.; Hautier, G.; Kochner, M.; Cholia, S.; Gunter, D.; Chevrier, V. L.; Persson, K. A.; Ceder, G. Python Materials Genomics (Pymatgen): A Robust, Open-Source Python Library for Materials Analysis. *Comp. Mater. Sci.* **2013**, *68*, 314–319.

(59) Wang, L.; Maxisch, T.; Ceder, G. Oxidation Energies of Transition Metal Oxides within the GGA+U Framework. *Phys. Rev. B* **2006**, *73*, 195107.

(60) Yu, L.; Zunger, A. Identification of Potential Photovoltaic Absorbers Based on First-Principles Spectroscopic Screening of Materials. *Phys. Rev. Lett.* **2012**, *108*, 068701.

(61) Zacharias, M.; Patrick, C. E.; Giustino, F. Stochastic Approach to Phonon-Assisted Optical Absorption. *Phys. Rev. Lett.* **2015**, *115*, 177401.

(62) Zacharias, M.; Giustino, F. One-Shot Calculation of Temperature-Dependent Optical Spectra and Phonon-Induced Band-Gap Renormalization. *Phys. Rev. B* **2016**, *94*, 075125.

(63) Bellaiche, L.; Vanderbilt, D. Virtual Crystal Approximation Revisited: Application to Dielectric and Piezoelectric Properties of Perovskites. *Phys. Rev. B* **2000**, *61*, 7877–7882.

(64) Stevanovic, V.; Lany, S.; Zhang, X.; Zunger, A. Correcting Density Functional Theory for Accurate Predictions of Compound Enthalpies of Formation: Fitted Elemental-Phase Reference Energies. *Phys. Rev. B* **2012**, *85*, 115104.

(65) Wang, L.; Maxisch, T.; Ceder, G. A First-Principles Approach to Studying the Thermal Stability of Oxide Cathode Materials. *Chem. Mater.* **2007**, *19*, 543–552.

(66) Hautier, G.; Ong, S. P.; Jain, A.; Moor, C. J.; Ceder, G. Accuracy of Density Functional Theory in Predicting Formation Energies of Ternary Oxides from Binary Oxides and its Implication on Phase Stability. *Phys. Rev. B* **2012**, *85*, 155208.

(67) Wang, L. F.; Rondinelli, J. M. Electrochemical Phase Diagrams for Ti Oxides from Density Functional Calculations. *Phys. Rev. B* **2015**, *92*, 245126.

(68) Tsuchiya, T.; Tsuchiya, J.; Umemoto, K.; Wentzcovitch, R. M. Phase Transitions in $MgSiO_3$ Perovskite in the Earth's Lower Mantle. *Earth and Planetary Sci.* **2008**, *224*, 241–248.

(69) Wang, S.; Kemper, A. F.; Baldini, M.; Shapiro, M. C.; Riggs, S. C.; Zhao, Z.; Liu, Z.; Devereaux, T. P.; Geballe, T. H.; Fisher, I. R. et al. Bandgap Closure and Reopening in $CsAuI_3$ at High Pressure. *Phys. Rev. B.* **2014**, *89*, 245109.

(70) Xiao, Z.; Du, K.-Z.; Meng, W.; Mitzi, D. B.; Yan, Y. Chemical Origin of the Stability

Difference Between Cu(I)- and Ag(I)-Based Halide Double Perovksites. *Angew. Chem.* **2017**,

(71) Zheng, C.; Rubel, O. Ionization Energy as a Stability Criterion for Halide Perovskites. *J. Phys. Chem. C* **2017**, *121*, 11977–11984.

(72) Rost, C. M.; Sachet, E.; Borman, T.; Moballegh, A.; Dickey, E. C.; Hou, D.; Jones, J. L.; Curtarolo, S.; Maria, J.-P. Entropy-stabilized oxides. *Nat. Commun.* **2015**, *6*, 8485.

(73) Butler, K. T.; Walsh, A.; Cheetham, A. K.; Kieslich, G. Organised Chaos: Entropy in Hybrid Inorganic-Organic Systems and Other Materials. *Chem. Sci.* **2016**, *7*, 6316.

(74) Zunger, A.; Wei, S.; Ferreira, L.; Bernard, J. Special Quasirandom Structures. *Phys. Rev. Lett.* **1990**, *65*, 353–356.

(75) Sanchez, J. M.; Ducastelle, F.; Gratias, D. Generalized Cluster Description of Multicomponent Systems. *Physica A* **1984**, *128A*, 334–350.

(76) Chevrier, V. L.; Hautier, G.; Ong, S. P.; Doe, R. E.; Ceder, G. First-Principles Study of Iron Oxyfluorides and lithiation of FeOF. *Phys. Rev. B* **2013**, *87*, 094118.

(77) Richards, A. University of Oxford Advanced Research Computing. http://dx.doi.org/10.5281/zenodo.22558, 2015.